Article

Structure

Distinct Allosteric Networks Underlie Mechanistic Speciation of ABC Transporters

Graphical Abstract

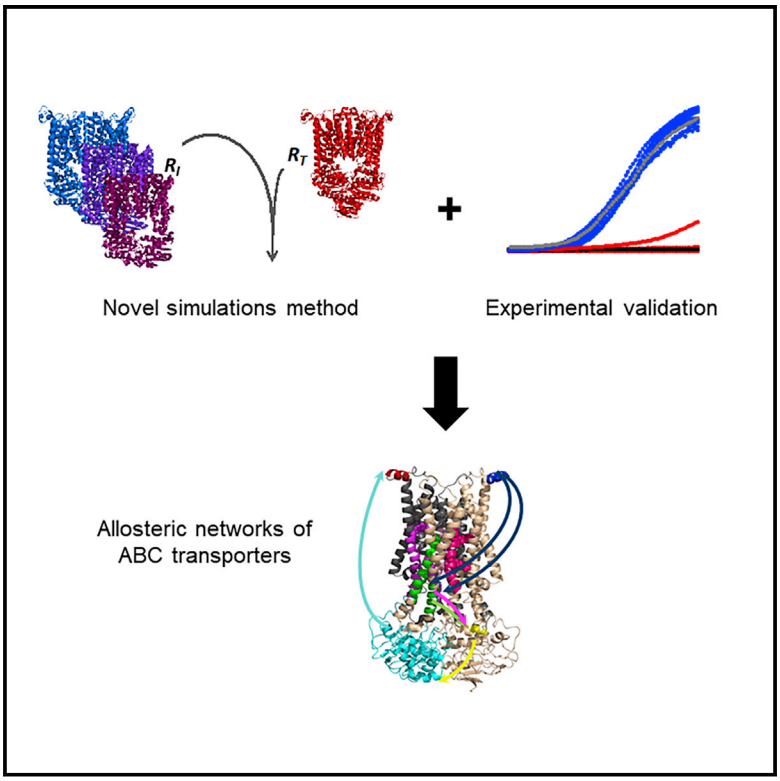

Highlights

- A method is developed to study allosteric communications in ABC transporters
- The outcome of engineered mutations is computationally predicted
- Experiments show that the predictions are highly accurate
- Different allosteric pathways give rise to different transport mechanisms

Authors

Burçin Acar, Jessica Rose, Burcu Aykac Fas, Nir Ben-Tal, Oded Lewinson, Turkan Haliloglu

Correspondence

lewinson@technion.ac.il (O.L.), turkanhaliloglu@gmail.com (T.H.)

In Brief

Long-range allosteric communication are essential to the function of molecular machines. Here, Acar et al. studied long-range communications in ABC transporters, and discovered that, despite the similar architecture of the transporters, each uses a very different communications network that is fine-tuned to its specific physiological role.

Acar et al., 2020, Structure *28*, 1–13
June 2, 2020
https://doi.org/10.1016/j.str.2020.03.014

CellPress

Please cite this article in press as: Acar et al., Distinct Allosteric Networks Underlie Mechanistic Speciation of ABC Transporters, Structure (2020), https://doi.org/10.1016/j.str.2020.03.014

Structure
Article

Distinct Allosteric Networks Underlie Mechanistic Speciation of ABC Transporters

Burçin Acar,[1,4] Jessica Rose,[2,4] Burcu Aykac Fas,[1] Nir Ben-Tal,[3] Oded Lewinson,[2,5,6,*] and Turkan Haliloglu[1,5,*]
[1]Department of Chemical Engineering and Polymer Research Center, Bogazici University, Istanbul, Turkey
[2]Department of Biochemistry and the Rappaport Institute for Medical Sciences, Faculty of Medicine, The Technion-Israel Institute of Technology, Haifa, Israel
[3]Department of Biochemistry and Molecular Biology, George S. Wise Faculty of Life Sciences, Tel Aviv University, Tel Aviv 69978, Israel
[4]These authors contributed equally
[5]These authors contributed equally
[6]Lead Contact
*Correspondence: lewinson@technion.ac.il (O.L.), turkanhaliloglu@gmail.com (T.H.)
https://doi.org/10.1016/j.str.2020.03.014

SUMMARY

ABC transporters couple the energy of ATP hydrolysis to the transmembrane transport of biomolecules. Here, we investigated the allosteric networks of three representative ABC transporters using a hybrid molecular simulations approach validated by experiments. Each of the three transporters uses a different allosteric network: in the constitutive B12 importer BtuCD, ATP binding is the main driver of allostery and docking/undocking of the substrate-binding protein (SBP) is the driven event. The allosteric signal originates at the cytoplasmic side of the membrane before propagating to the extracellular side. In the substrate-controlled maltose transporter, the SBP is the main driver of allostery, ATP binding is the driven event, and the allosteric signal propagates from the extracellular to the cytoplasmic side of the membrane. In the lipid flippase PglK, a cyclic crosstalk between ATP and substrate binding underlies allostery. These results demonstrate speciation of biological functions may arise from variations in allosteric connectivity.

INTRODUCTION

ABC transporters are members of an ancient superfamily of transport proteins that play diverse and vital roles in all kingdoms of life (Higgins, 1992; Dassa and Bouige, 2001; Holland et al., 2003). These membrane-embedded enzymes couple the energy of ATP hydrolysis to the transport of a wide range of biomolecules (ter Beek et al., 2014; Locher, 2016; Lewinson and Livnat-Levanon, 2017). They act as cellular membrane gatekeepers, allowing passage of various substrates into or out of cells or cellular organelles, thus regulating intracellular concentrations of biomolecules. ABC transporters are tightly linked to human diseases, tumor resistance to chemotherapy, and bacterial virulence (Gottesman et al., 2002; Riordan, 2008; McDevitt et al., 2011; Remy et al., 2013; Tanaka et al., 2018; Thomas and Tampé, 2018). ABC transporters share a common architecture and are minimally composed of two intracellular nucleotide-binding domains (NBDs) that bind and hydrolyze ATP, and two transmembrane domains (TMD) that form a permeation pathway. ABC transporters that function as importers additionally require a substrate-binding protein (SBP) which recognizes the substrate with high affinity and delivers it to the TMD (Karpowich et al., 2003; Berntsson et al., 2010; Fulyani et al., 2013).

It is broadly recognized that long-range allosteric communications are essential to the function of proteins (Dokholyan, 2016; Wodak et al., 2019). In ABC transporters, ATP binding and hydrolysis at the NBD are coupled to the conformational changes of TMDs that shift between the inward- and outward-facing conformations (Johnson and Chen, 2018; Kim and Chen, 2018; Nguyen et al., 2018). Concomitantly, docking and undocking of the SBP to the extracellular side of the TMD modulates ATP hydrolysis at the NBD, occurring 60–70 Å away (Davidson et al., 1992; Ames et al., 1996). These allosteric communications are essential for the synchronized movements of distant protein domains that result in unidirectional transport.

Despite the understanding that allosteric communications underlie the transport mechanism of ABC transporters, little is known about the molecular basis of this phenomenon: What are the driving events, and what are the driven ones? Where does the allosteric signal start? How is it propagated? Are there essential amino acids that relay the signal? Do different ABC transporters have similar allosteric networks? The experimental exploration of such questions is very challenging and is therefore often investigated by computational methods. Indeed, allostery and conformational changes of ABC transporters have been computationally studied in the past and have led to important insights (Jones and George, 2002; Oloo and Tieleman, 2004; Aittoniemi et al., 2010; Oliveira et al., 2011; Proctor et al., 2015).

Recently, single-molecule techniques demonstrated that the conformational changes of the ABC transporter BtuCD occur on a timescale of hundreds of milliseconds to several seconds (Goudsmits et al., 2017; Yang et al., 2018), considerably longer than the duration of current molecular dynamics (MD) simulations. Sampling enhancement methods (e.g., metadynamics, umbrella sampling, replica exchange) could be suitable for such long timescales, but their application for large proteins, such as ABC transporters is highly demanding computationally

(Bernardi et al., 2015; Maximova et al., 2016). Therefore, we developed a novel hybrid molecular simulation methodology that identifies the most probable conformational trajectory between two known protein structures.

This approach, termed ANM-LD, holds several important advantages over existing molecular simulations approaches (for a comprehensive description of method development and validation see the Supplemental Information and Figure S1).

ANM-LD integrates low-resolution α carbon-based anisotropic network model (ANM) (Atilgan et al., 2001) with stochastic all-atom implicit solvent Langevin dynamics (LD) simulations (Brünger et al., 1984). The low-resolution (yet computationally economic) method is used to limit the conformational space that needs to be searched by the high-resolution (and computationally demanding) method. Therefore, this combination allows the time-efficient simulation of large and complex proteins. No extrinsic bias is used to drive the protein from one conformation to the other: ANM-LD is guided solely by the intrinsic dynamic modes of motion that are accessible to the protein. As exemplified herein, another advantage of ANM-LD is its ability to infer causality (driver-driven) relations of long-range allosteric interactions. Finally, ANM-LD provides a platform to accurately predict the results of mutations.

Herein, we combined ANM-LD simulations and functional assays to study conformational changes and allosteric communication in three subgroups of ABC transporters: type I and type II ABC importers and ABC exporters. As representatives of ABC importers, we chose the *E. coli* ABC transporters for maltose (MalFGK) and for vitamin B_{12} (BtuCD), which are the best-characterized members of the type I and II subgroups (respectively) and have been shown to operate by very distinct mechanisms (Lewinson et al., 2010; Vigonsky et al., 2013). To represent the exporter subgroup, we chose PglK, the ATP-driven lipid-linked oligosaccharide flippase. PglK has been proposed to operate by a mechanism that is fundamentally different from that described for all other ABC transporters, where the substrate never fully enters the transmembrane translocation cavity and the transporter remains in the outward-facing conformation throughout the transport cycle (Perez et al., 2015). We chose three such mechanistically diverse ABC transporters to examine the correlation between allosteric connectivity and mechanism of action.

RESULTS

ANM-LD Captures Meaningful Dynamic Information from Static Crystal Structures

We first tested whether ANM-LD can capture dynamic information that is not evident in the static structures, yet is consistent with previous experimental studies. For this, we used the published structures of the vitamin B_{12} importer in its APO (Locher et al., 2002), ATP-bound (Korkhov et al., 2014), BtuF-bound (Hvorup et al., 2007), and ATP/BtuF-bound (Korkhov et al., 2012) states and simulated the conformational trajectories between these structures. For initial analysis of the simulations, we calculated the mean square fluctuations (MSFs) for each residue of BtuCD, in each of the conformational transitions. Rather than measuring the positional difference between initial and target conformations, MSF is a measure of how much a residue fluctuates during the simulation. To emphasize the difference between MSF and positional difference, one may consider the complete conformational cycle of a transporter (or an enzyme). Upon completion of the cycle and return to the resting state, the positional displacement of all residues will be zero, while the MSF will greatly differ and will depend on how much each residue moved during the catalytic cycle. As shown, docking of BtuF to APO BtuCD had almost no effect on the mobility of NBD-located residues and mainly increased the mobility of residues that comprise its own docking sites and of TMD residues that are located at the periplasmic side of the TMD (Figures 1A and S2A). These observations are in line with experimental data that demonstrate that docking of BtuF induces conformational changes predominantly at the periplasmic side of the TMD (Joseph et al., 2011, 2014), and has little effect on ATP hydrolysis rates (Borths et al., 2005; Tal et al., 2013). Not surprisingly, ATP binding increased the mobility of many of the residues that comprise the ATP-binding site. Less expectedly, and unlike the localized effects of BtuF, the effects of ATP binding extended also to the TMD (Figures 1B and S2B), inducing mobility in the cytoplasmic side of several TMD helices (helices 4, 5, 7, 8, and 10). This ATP-induced mobility of TMD residues is consistent with EPR/DEER and single-molecule spectroscopic measurements (Joseph et al., 2011, 2014; Yang et al., 2018). Remarkably, binding of ATP also enhanced the mobility of residues that are located ~60–65 Å away from the ATP-binding site; the majority of which are involved in docking of BtuF (Figure 1B).

When BtuF docks to ATP-bound BtuCD, it augments the ATP-induced mobility in residues that comprise its own docking site and in ones that comprise the periplasmic gate (Figures 1C and S2C). A similar BtuF-augmenting effect is revealed by comparing the mobility patterns of the APO with the ATP-bound transition with those of the APO with the ATP + BtuF transition. The two mobility patterns are similar in general, yet the mobility of TMD residues induced by ATP binding is further extended (Figures 1B and 1D) and increased (Figures S2B and S2D) by docking of BtuF.

We find it encouraging that by using only the static crystal structures this preliminary analysis of the ANM-LD simulations recapitulated experimentally determined dynamic features of BtuCD (Borths et al., 2005; Joseph et al., 2011, 2014; Tal et al., 2013; Yang et al., 2018).

The Allosteric Network of BtuCD

In ABC transporters, distant domains allosterically communicate and transmit information regarding the nucleotide state of the NBD, docking and undocking of the SBP and conformational state of the TMD (ter Beek et al., 2014; Locher, 2016; Lewinson and Livnat-Levanon, 2017). This allosteric communication is essential for the synchronization between ATP hydrolysis, conformational changes, opening and closing of gates, and ultimately for transport. To understand the allosteric connectivity that underlies the transport mechanism, we analyzed the degree of correlated movements between all of the residues of BtuCD. At the basis of this analysis is the assumption that residues that are allosterically connected will move along parallel vectors in both space and time. An extreme example of such synchronization is the perfect correlation of each residue with itself, represented by the diagonal of the 2D correlations maps (Figures 2A and 2B). Similarly, two residues that are sequential in the amino

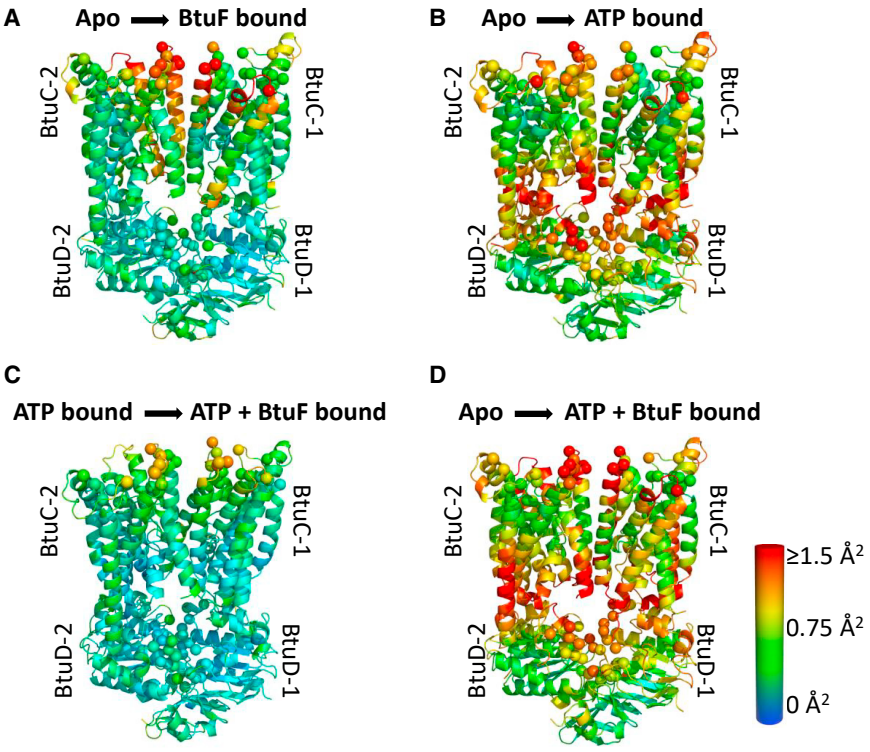

Figure 1. Mobility of BtuCD Residues during the Conformational Cycle

The mean square fluctuations (MSF) (red, high; blue, low) of every residue in each of the indicated (A–D) conformational transitions is shown on a ribbon representation of BtuCD. ATP- and BtuF-binding residues are shown as spheres.

acid sequence will also display high correlation. However, when highly correlated movements are observed for residues or domains that are distant in sequence and in 3D space, this likely represents an allosteric connection.

The 2D correlation map of the transition from the APO to the BtuF-bound state is dominated by cyan, green, and yellow colors signifying weak correlations (Figure 2A). This suggests that docking of BtuF does not elicit long-range allosteric interactions in the transporter. In contrast to the weak allosteric connectivity induced by docking of BtuF, binding of ATP induces strong global positive and negative correlation of movements in both the TMD and NBD (Figure 2B). These correlations are both internal within each domain (NBD or TMD), but are also between the different domains (i.e., between BtuC-1 and BtuD-1 and between BtuC-2 and BtuD-2, Figure 2B). Thus, upon binding of ATP, the motions of BtuCD become more synchronized, with each domain moving more as a single dynamic unit, in coordination with the other domains. In addition to these global effects, binding of ATP also induces strong communication between specific distant functional domains. For example, it increases the correlation between residues involved in ATP binding and those that form the BtuF-docking site, and between the ATP-binding sites and the cytoplasmic gates and coupling helices (Figure 2B). Such long-range allosteric interactions between specific functional sites are difficult to deduce from static crystal structures, but are nevertheless expected to exist according to the accepted mechanistic models of BtuCD (ter Beek et al., 2014; Locher, 2016; Lewinson and Livnat-Levanon, 2017; Yang et al., 2018). The identification of these allosteric interactions between experimentally identified functional sites is testimonial for the usefulness of the ANM-LD approach.

Although the effects of ATP are more comprehensive than those of BtuF, the SBP has important fine-tuning roles. In concert with ATP, docking of BtuF increases the internal cooperativity of each TMD, and to a lesser extent of each NBD (Figure S3), meaning that BtuF increases the synchronization of intra-domain movements. In addition, docking of BtuF extends the reaches of the TMD-NBD cooperativity toward the periplasm (Figure S3). Perhaps the most striking effect of BtuF is on the pore-lining TM helices 5a and 5b (Figures 2C and 2D). When ATP binds in the absence of BtuF, the movement of TMD helices 5a and 5b is positively correlated in space and time (Figure 2C). This means that if one of these helices fluctuates in one direction the other will fluctuate in the same direction at the same time. Thus, the distance between TMD helices 5a and 5b remains constant keeping the translocation pathway closed. In contrast, binding of ATP in the presence of BtuF leads to a reversal of the dynamic correlation between the two pore-lining helices, which now become strongly negatively correlated (Figure 2D). This means that if one of these helices fluctuates to the right, the other will fluctuate to the left. This antiparallel (yet synchronized) correlation of movements of helices 5a and 5b results in opening of the translocation pathway to allow passage of vitamin B_{12}. Collectively, these results demonstrate that ATP binding is the major driving force for cooperative allosteric connectivity in BtuCD-F. However, BtuF acts as a "fine-tuner," augmenting the effects of ATP, extending the reach of the cooperativity induced by it, and has specific local effects that are essential to the transport cycle.

Experimental Validation of the ANM-LD Simulations

Next, we tested whether we can use the ANM-LD simulations to computationally predict which mutations will impair the transport activity of BtuCD (and which will not), and then experimentally test these predictions. The approach used for the analysis of the mutations is depicted in Figure S4A and described in detail in the STAR Methods, while below it is explained more concisely.

The first step of this analysis is to identify the most fundamental "modes" of motion utilized by BtuCD: in ANM-LD, the simulation advances in discrete iterative steps from the initial to the final conformation. In each such iterative step the algorithm attempts to reach as close as possible to its target conformation by choosing a certain mode of motion that abides by the biophysical, biochemical, and dynamic constraints of the protein polymer. As a result, the modes of motion that are chosen by the

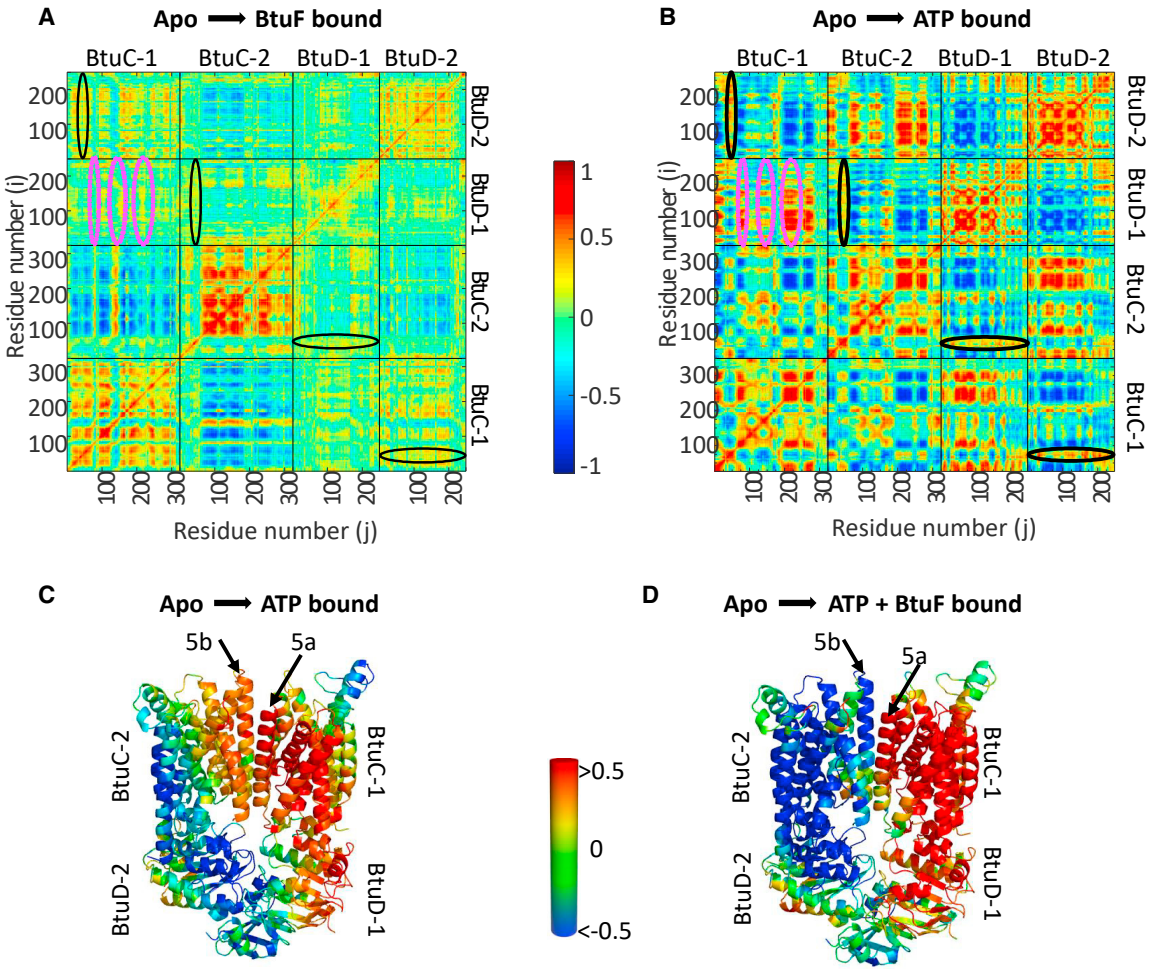

Figure 2. Binding of ATP to BtuCD Leads to Stronger Correlated Movements than Binding of BtuF

(A and B) Shown are the dynamic cross-correlation maps between all residues of BtuCD upon binding of BtuF (A) or ATP (B). Red colors indicate strong positive correlation, meaning that the residues travel in parallel vectors in space and time, blue colors indicate negative correlation. Black ovals highlight the weak (A, BtuF binding) and strong (B, ATP binding) correlation between BtuF-docking residues (in the TMD) and ATP-binding residues (in the NBD). Magenta ovals highlight the weak (A, BtuF binding) and strong (B, ATP binding) correlation between NBDs, cytoplasmic gates, and coupling helix.

(C and D) The role of BtuF: opening of the translocation pore. Shown is a ribbon representation of APO BtuCD, where each residue is colored according to its correlated movement with M160 of the pore-lining helix 5a. When only ATP binds (C), the pore-lining helices 5a and 5b are positively correlated, meaning that the translocation pathway remains closed. When BtuF binds in concert with ATP (D), helices 5a and 5b become negatively correlated, and the translocation pathway would open.

algorithm in the early steps of the simulation encompass global and highly cooperative conformational changes, which are historically termed ''slow modes.''

In parallel simulations, we repeatedly observed several major modes of motion that underlie the conformational transition from the APO to the ATP/BtuF-bound state. The first of these modes of motion corresponds to the antiparallel rotation of the NBD and the TMD (Video S1). The second mode of motion corresponds to the movement of the periplasmic region that leads to opening of the translocation channel (Video S2). The third mode corresponds to a squeeze and release movement of BtuCD along the vertical axis, comprising the closing and opening of the NBDs, opening/closing of cytoplasmic gates, and expansion/constriction of the periplasmic gate (Video S3). Finally, the fourth movement couples the closure of the NBD with the opening of the periplasmic gate and closure of the cytoplasmic gate (Video S4).

Next, we wished to detect the hinge residues that enable each of these modes of motions. For this, we mapped these four ANM modes onto a 1D dynamic space defined by the Gaussian Network Model (GNM) (Bahar et al., 1997; Haliloglu et al., 1997) based on their similarity to GNM mode shapes. GNM, with its underlying energy function, is a very robust method to identify the hinge residues of a certain mode of motion (Cui and Bahar, 2006; and see the STAR Methods). By using this combination of ANM-LD and GNM we identified the positions of 15 amino acids that serve as important hinges for the motions of BtuCD (Figure S5A).

Subsequently, for each of these 15 positions we chose an amino acid substitution that we anticipated would compromise

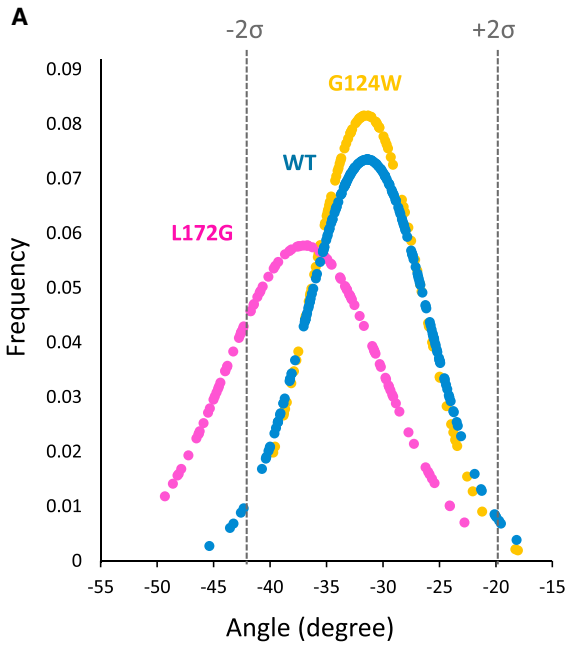

Figure 3. Computational Prediction of the Effect of Point Mutations

(A) An example of the distribution of one rotational angle (ϕ272), between the plane formed by the α carbons of amino acids 272, 273, 274, and the plane formed by the α carbons of amino acids 273, 274, 275. Each data point represents a value of ϕ272 in one of the 100 steps (cycles) of the simulation of the conformational change between the APO and the ATP/BtuF-bound states. As shown, the distribution of ϕ272 of mutant G124W is very similar to that of WT BtuCD, while that of mutant L172G is broader and extends to angles not sampled by the WT protein.

(B) Shown are the angular deviation (AD) values calculated for the *in silico* mutants. Mutants with relatively low AD values (e.g., A121H) are predicted to follow a trajectory of conformational changes that is similar to WT BtuCD, while those with relatively high AD values (e.g., L90R) are predicted to follow a conformational trajectory that is different from that of the WT protein. The mutants in (B) are color-coded according to their experimentally determined activity (blue, active; red, inactive; see below).

its hinge function by altering its characteristics and/or its interactions with its neighboring residues. To increase the likelihood that the effect of the mutation would be observed in our computations and detected in our experiments we started with radical mutations. For example, substitution of a small Gly by a rigid Trp or vice versa, or abolishing/reversing the charge of Asp or Glu residues.

We next exploited the time efficiency of the ANM-LD approach to simulate the conformational transitions of the mutants. To evaluate the effects of the mutations we compared the conformational trajectory of the mutants with that of wild-type (WT) BtuCD. For this comparison we calculated the bond/backbone rotation angles (φ) between the plane formed by three consecutive Cα carbons ($C\alpha_i$, $C\alpha_{i+1}$, and $C\alpha_{i+2}$) and the plane generated by the next three Cα carbons ($C\alpha_{i+1}$, $C\alpha_{i+2}$, and $C\alpha_{i+2}$) (Figure S4B).

To determine how one such angle changes during the conformational transition, its value was calculated for each of the 100 steps of the simulation. Figure 3A shows an example of the distribution of one such rotational angle formed between the Cα carbons of residues 272–275. As shown, the distribution of φ_{272} of mutant G124W is very similar to the WT protein, while mutant L172G displays a very different distribution. To economize the calculations comparing the bond angles of WT and mutant BtuCD, instead of calculating all of the bond rotation angles we focused on the 57 rotational bond angles that are at or nearest (in either sequence or 3D space) to the hinge residues of the most frequently used mode of motion (ANM-1, Video S1), which is the most frequently used and most collective of all modes. In restricted runs (see the STAR Methods) where this mode was disallowed the simulation failed to approach the target conformation, suggesting that ANM-1 is essential for the conformational change, and any mutant unable to perform this mode of motion is bound to lose its activity. Therefore, for each mutant we now had a quantitative description of how the 57 rotational bond angles comprising ANM-1 change during the conformational transition, essentially generating a conformational trajectory "fingerprint." To quantitatively compare the fingerprint of a given mutant with that of the WT protein, we summed the deviations of the rotational angles (φ) of the mutant from the means of the rotational angles of WT BtuCD (μ_{WT}), summed over all the ANM-LD steps and for all the 57 rotational bond angles (Equation 1).

$$AD(mutant) = \sum_{\substack{ANM1 \\ hinge\ res}} \sum_{frames} | \times (\varphi_{mutant}(resno, frame) - \mu_{WT}(resno, frame)) | \quad \text{(Equation 1)}$$

This sum of angular deviations from WT provides a score of how much the conformational transition trajectory of a given mutant differs from that of WT BtuCD. Figure 3B shows the angular deviation values calculated for the BtuCD mutants, each harboring a single point mutation in one of the predicted hinge positions. Our expectation was that high angular deviation scores would be associated with inactive mutants, while the lower angular deviation scores would be associated with mutants that retained transport activity.

To experimentally test this prediction we used site-directed mutagenesis and generated these 15 point mutations. The correct insertion of all mutants, and lack of off target effects were verified by sequencing. We then tested the membrane fraction expression level of the mutants and proceeded to analyze only mutants that showed WT-like expression (Figures S5B and S5C, and not shown).

To test the activity of the mutant variants we used an *in vivo* vitamin B_{12} uptake assay, where *E. coli* cells are grown under conditions that require high-affinity uptake of vitamin B_{12} (Cadieux et al., 2002; Tal et al., 2013). Under these conditions, only cells that express functional BtuCD can grow. As shown in Figure 4A, *btuCD*-deleted cells indeed did not grow under

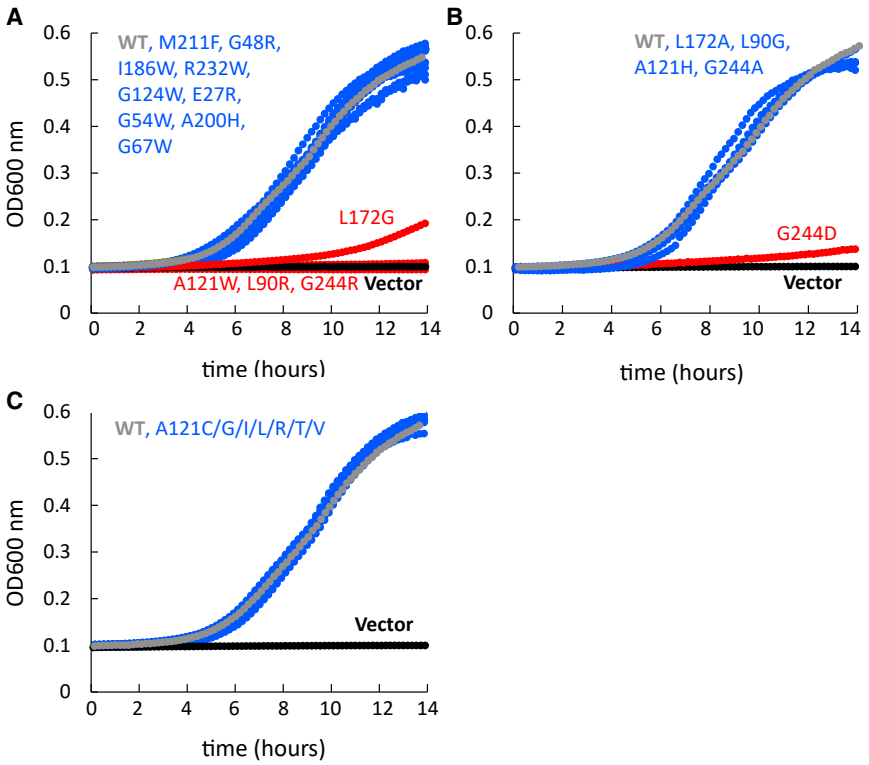

Figure 4. Experimental Evaluation of Mutants

Cells were grown under conditions that require the high-affinity uptake of vitamin B12 (see the STAR Methods). Shown are representative results of experiments repeated at least three times. Curves that are colored in the same color did not significantly differ.

(A) Growth of the initial set of 13 mutants. As shown, cells transformed with an empty vector (black trace) failed to grow while those transformed with a plasmid harboring WT BtuCD (gray) grew normally. Four of the tested mutants (L172G, A121W, L90R, G244R; red curves) partially or fully failed to grow. The growth of the other nine mutants (blue curves) was considered similar to that of cells expressing WT BtuCD.

(B) Same as (A), only shown is the growth of the active counterparts (L172A, L90G, and A121H, blue curves) of the inactive mutants identified in (A). Also shown is mutant G244D, the only mutant for which we observed a discrepancy between predicted and experimental results.

(C) Same as (A), only shown is the growth of the panel of the active A121 variants (blue curves).

these conditions, unless transformed with a plasmid encoding WT BtuCD. Next, we tested growth-complementation by the point mutants for which we performed bond rotational angle analysis. Of the 13 mutants that displayed WT-like expression levels, 9 complemented the growth of the *btuCD*-deleted strain (Figure 4A, blue curves), demonstrating that these mutations did not significantly alter the transport activity of BtuCD. Interestingly, these 9 active mutants had the lowest computed angular deviation scores (Figure 3B, blue circles). The remaining four mutations fully (L90R, A121W, and G244R) or partially (L172G) abrogated the vitamin B_{12} uptake activity of BtuCD, despite having WT-like levels of membrane fraction expression (Figures S5B and S5C). Quite remarkably, the four mutants that compromised the activity of BtuCD (L90R, A121W, L172G, and G244R; Figure 4A, red curves) had the highest angular deviation scores (Figure 3B, red circles).

Subsequently, for the four mutations that led to reduced activity we attempted to computationally identify other mutant variants, ones with bond angular distributions that are more similar to WT BtuCD. We found that mutants L90G, A121H, L172A, G244D, and G244A had a lower angular deviation score than their inactive counterparts (Figure 3B, compared with scores of L90R, A121W, and L172G). Consistent with their lower angular deviation scores, mutants L90G, A121H, L172A, and G244A fully complemented the growth of the *btuCD*-deleted strain (Figure 4B). Mutant G244D did not behave as expected: its angular deviation score was relatively low (Figure 3B), yet this mutation almost completely abrogated vitamin B_{12} uptake activity (Figure 4B). We speculate that such a discrepancy may arise from the nature of the effect of some mutations that introduce local perturbations without affecting the overall conformational trajectory (as represented by the angular deviation score calculations). Such local perturbations may interfere with gating, substrate interactions, interactions with the SBP, or local helix packing; with the latter offering a plausible explanation in the case of the G244D mutation.

The angular deviation score of mutant A121H was the lowest we had observed so far, indicating that this mutant is very similar to WT BtuCD. In an attempt to identify additional A121 variants with greater deviation from WT score we generated (*in silico*) seven other substitutions in this position (A121C/G/I/L/R/T/V). We then ran simulations for these mutants, and calculated their angular deviation scores. As shown in Figure 3B, the angular deviation scores of these seven mutants were lower than those of the inactive mutants (L90R, L172G, A121W) and also lower than that of fully active mutant I186W. Based on these computational results we expected that mutations A121C/G/I/L/R/T/V would not abolish the transport activity of BtuCD. To test this, we generated these mutants by site-directed mutagenesis and assessed their activity. As shown (Figure 4C), in line with the ANM-LD predictions, all of the seven mutants fully complemented the vitamin B_{12}-dependent growth of the *btuCD*-deleted strain.

In conclusion, for 25 (out of 26) point mutations we observed a very good correlation between the ANM-LD predictions (angular deviation scores) and the *in vivo* vitamin B_{12} uptake assay.

The effects of point mutations are routinely predicted by calculating their effect on protein stability (Yin et al., 2007; Worth et al., 2011; Montanucci et al., 2019). To compare the angular deviation calculations with predictions that are based on stability calculations we used FoldX (Schymkowitz et al., 2005) and calculated the $\Delta\Delta G$ of the mutations for both the initial (apo) and target (ATP/BtuF-bound) conformations (PDB: 1L7V and 1FI3, respectively). As shown in Figure S6, in both conformations the calculated $\Delta\Delta G$ of the mutants was not a good predictor of activity.

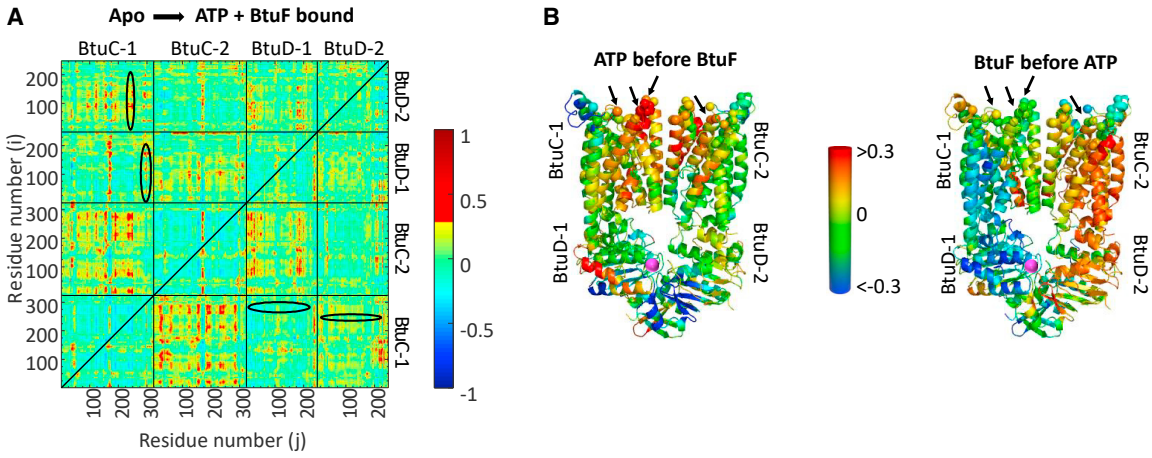

Figure 5. Kinetics of Allosteric Relations between BtuF and ATP in BtuCD

(A) Shown is the time-delayed dynamic cross-correlation map for the transition from the APO to the ATP + BtuF conformation. A time delay (τ) of 40 cycles (out of a 100 necessary to complete this transition) was imposed between residues i (vertical axis) and residues j (horizontal axis). As shown (black ovals at upper left quadrants), when the ATP-binding sites fluctuate at time t, the BtuF-docking sites show strong correlated movements at the later time ($t + \tau$). When the temporal order is reversed and the BtuF-docking sites fluctuate first, the ATP-binding sites show no correlation of movements at time = $t + \tau$ (black ovals at lower right quadrants).

(B) A structural representation of the kinetic relations in BtuCD. Shown is a ribbon representation of APO BtuCD, where each residue is colored according to its time-delayed correlation with the ATP-binding residue A163 (magenta sphere). As shown in the left panel, when the fluctuations in A163 (i.e., in the ATP-binding site) precede, the BtuF-docking sites (indicated by arrows) show strong positive correlation at a later time ($t + \tau$, $\tau = 40$). However, when the order is reversed (right panel) and the BtuF-docking sites fluctuate first, this positive correlation between binding of ATP and BtuF is lost.

Inferring Causality of Allosteric Interactions: Who Is Driving and Who Is Driven?

The ANM-LD simulations offer an opportunity to examine mechanistic features that are difficult to determine experimentally. One such feature is the pre-equilibrium kinetics of allosteric interactions: if residues A and B are allosterically connected, does the conformational change of A follow that of B, or vice versa? In other words, who is driving and who is driven? To investigate these driver-driven relations in BtuCD-F, we re-analyzed the simulations while imposing a time delay (expressed as cycles of the simulation) between the conformational changes of allosterically coupled residues (or a domains) of interest. For any two allosterically coupled residues, if the change in A drives that of B, A's movement must precede B's. If we impose that the conformational change in A occurs before that of B, and still observe a positive correlation in the 2D correlations map, this means that the conformational change of A precedes (and drives) that of B. If the correlation is lost, this means that B likely drives A, which can be confirmed by imposing the opposite time delay (i.e., imposing that the change in B precedes) and verifying that the positive correlation is again observed (for more details, and for a mathematical expression of these relations, see the STAR Methods). We used these time-delayed correlations to determine if the conformational changes that occur in the ATP-binding residues precede (and thus trigger) those that occur in the residues that are involved in BtuF binding, or vice versa. The time-delayed cross-correlation maps demonstrate that when the ATP-driven conformational changes occur earlier the correlations persisted, yet disappeared when BtuF-driven conformational changes occur earlier (Figure 5A). For example, the correlation between the ATP-binding residue S163 (in the D loop of the NBD) and the periplasmic gate residues V170, R173, Q174, and Y177 is only present if the conformational change in S163 precedes that of V170, R173, Q174, and Y177 (Figure 5B).

Similarly, the BtuF-binding residues (residues L249, L298, and A300-L303) show high movement correlation with the ATP-binding sites (NBD), but only if their movement is preceded by that of the NBD-located residues (Figure S7). This means that the ATP-induced conformational changes occur before the BtuF-driven ones, and that binding of ATP initiates allosteric connectivity in BtuCD-F.

To further investigate the causality relations of allosteric communication in BtuCD we performed transfer entropy calculations (Hacisuleyman and Erman, 2017, and see the STAR Methods). The transfer of entropy from residue i to residue j leads to a decrease in the degree of uncertainty for residue j, i.e., the dynamics of i affects the dynamics of j. Using only the most fundamental modes of motion of BtuCD (Videos S1, S2, S3, and S4), we determined the transfer entropy that underlie these cooperative motions. As shown in Figure S8A, the ATP-binding sites in BtuCD decrease the uncertainty of motion of the BtuF-binding residues. This observation supports the notion that in BtuCD the dynamics of the ATP sites precedes, and that of the BtuF sites follow.

A Comparison with the Allosteric Connectivity in MalFGK and in PglK

ABC transporters sub-divide into several distinct subgroups, where each subgroup is characterized by a distinct structure and mechanism (Lanfermeijer et al., 1999; van der Heide and Poolman, 2000; Sebulsky et al., 2003; Lewinson et al., 2010; Vigonsky et al., 2013; Qasem-Abdullah et al., 2017). The differences

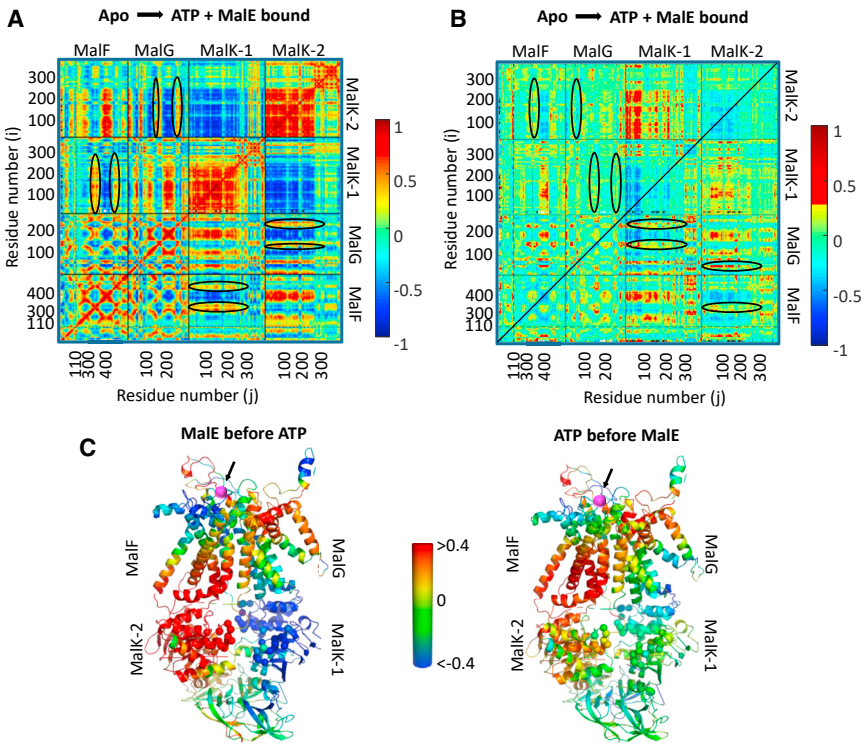

Figure 6. Allosteric Connectivity and Causality Relations in MalFGK

(A) Shown is the time-independent (no time delay) dynamic cross-correlation map for MalFGK conformational changes that occur during binding of ATP/MalE. The black ovals highlight the correlation between the MalF-located MalE-docking sites (including N341-F344, P365, N449, D453-P460, and R473-Q482) and the ATP-binding residues of MalK-1, and between the MalG-located MalE-docking sites (including V138, Y141, S234, R238, and Q250-N257) and the ATP-binding residues of MalK-2.

(B) Shown is the same dynamic cross-correlation map as in (A); however, a time delay (τ) of 25 cycles (out of a 50 necessary to complete this transition) was imposed between residues i (vertical axis) and residues j (horizontal axis), and the map shows the correlation of residue i at time t with residue j at a later time ($t + \tau$). As highlighted by the black ovals, the correlation between the MalE-docking sites and the ATP-binding residues is only present if MalE docking precedes (black ovals at lower right), and is lost if the ATP-binding residues fluctuate first (black ovals at upper left).

(C) A structural representation of the causality relations in MalFGK. Shown is a ribbon representation of APO MalFGK, where each residue is colored according to its time-delayed correlation (τ = 25) with Q41 of MalF (magenta sphere, arrow), which is part of the MalE-docking site. As shown, the correlation between the NBD of MalK-2 and this residue is very strong if MalE-docking precedes (left panel), yet is almost completely lost if ATP binding occurs first (right panel).

between the subgroups are arguably best exemplified by comparing BtuCD-F (type II sub-class [Hvorup et al., 2007]) with the maltose transporter (MalFGK-E, type I sub-class [Oldham and Chen, 2011]). To compare the allosteric network of BtuCD-F with that of MalFGK-E, we conducted ANM-LD simulations with the latter as well (see Supplemental Information for details). At first glance, the allosteric map of MalFGK appears quite similar to that of BtuCD: upon transition from the APO to the ATP- and MalE-bound state, the NBD (with the exception of the C-terminal regulatory domain) largely move as a single dynamic unit (Figure 6A). As in BtuCD, the TMDs are fragmented to smaller dynamic units, indicating that there are more hinges in the TMDs than in the NBDs. As in BtuCD, the 2D correlation map of MalFGK reveals the long-range allosteric crosstalk between the ATP-binding sites (at the NBD) and the MalE-docking sites (periplasmic site of the TMD) (Figure 6A). However, despite this similarity, important mechanistic differences are observed between BtuCD-F and MalFGK-E.

Overall, the TMDs of MalFGK are more mobile than those of BtuCD (Figures S8C and S8D). This is especially apparent in the SBP-docking sites, where the MalE-docking sites are much more mobile than their BtuF counterparts. These differences in the mobility of the docking sites for the SBPs indicate that docking of BtuF requires less rearrangement than is required for MalE, and suggest that, relatively, BtuF docks via a lock-and-key mechanism (geometrical complementarity) while MalE docks via an induced fit mechanism. This suggestion is likely related to the conformational changes that the SBPs undergo upon ligand binding: during the transport cycle, the SBP needs to dock in its HOLO form and undock in its APO form. In BtuF, the vitamin B_{12}-bound and -free conformations are similar (Karpowich et al., 2003), and thus the SBP-docking site requires little rearrangement between docking of the HOLO form of the SBP and release of its APO form. In contrast, MalE undergoes significant conformational changes upon binding of maltose (Sharff et al., 1992; Quiocho et al., 1997). Accordingly, significant conformational changes are required for the switch between docking of the substrate-loaded SBP and release of its APO form. Perhaps the most striking differences between the two ABC transporters lie in the kinetic/causality relations between binding of ATP and docking of the SBP. As described above (Figures 5, S2, S3, S7, and S8A), in BtuCD, binding and unbinding of ATP is the initiator event, and binding and unbinding of BtuF follows. This cause-and-effect relationship is reversed in MalFGK-E. Here, docking of MalE drives the conformational changes in its docking sites, which subsequently initiate the conformational changes in the ATP-binding sites (Figures 6B and 6C). Hence, in MalFGK, the initiator for the conformational changes is the SBP, while in BtuCD it is ATP. Similar conclusions were drawn from transfer entropy calculations of MalFGK. As shown in Figure S8B, the MalE-binding sites in MalFKG decrease the uncertainty of motion of the ATP-binding residues, suggesting that in MalFGK-E the dynamics of the MalE-docking sites precedes, and that of the ATP sites follow. These kinetic/causality differences between MalFGK and BtuCD are well correlated with the different mechanism used by each system: in MalFGK, the

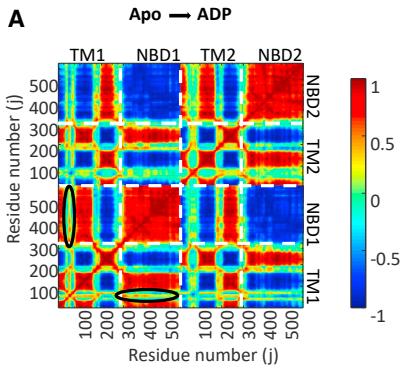

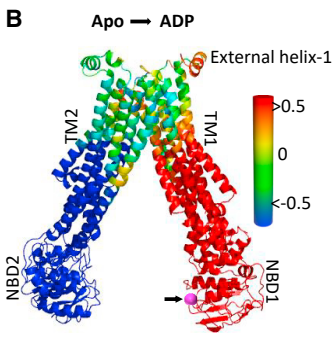

Figure 7. Allosteric Connectivity in PglK

(A) Shown is the time-independent (no time delay) dynamic cross-correlation map for the PglK conformational changes that occur during binding of ADP. The black boxes highlight the correlations between the external helix and the NBD of the same chain.

(B) A structural representation of the allosteric connectivity in PglK. Shown is a ribbon representation of APO PglK, where each residue is colored according to its correlation with G385 on NBD-1 (magenta, arrow). As shown, external helix 1 displays positive correlation with NBD-1.

ATP-binding sites do not form unless maltose-loaded MalE docks (Oldham et al., 2007; Orelle et al., 2008). Consequently, the basal ATP hydrolysis rate of MalFGK is very low and is greatly stimulated by docking of maltose-bound MalE (Davidson et al., 1992). In contrast, in BtuCD, binding of ATP is sufficient to induce the formation of the ATP-binding sites, and this event is BtuF independent (Yang et al., 2018). Consequently, the basal ATP hydrolysis rate of BtuCD is high and is only mildly stimulated by BtuF (Borths et al., 2005; Tal et al., 2013). We find it remarkable that the ANM-LD simulations capture the mechanistic difference between the systems.

The differences in the allosteric networks and causality relations between MalFGK and BtuCD prompted us to investigate another ABC transporter, PglK, a lipid-linked oligosaccharide flippase. PglK adopts the canonical exporter 3D fold that is very different from that of both MalFGK and BtuCD, and has been suggested to operate by an atypical transport mechanism where the substrate never fully enters the transmembrane translocation cavity, and the transporter remains in the outward-facing conformation during the transport cycle (Perez et al., 2015). To investigate the allosteric connectivity in PglK, we conducted ANM-LD simulations of the conformational transition between its inward-facing APO conformation and its outward-facing ADP-bound conformation (Perez et al., 2015).

The overall distribution of blue (negative correlation) and red (positive correlation) areas in the 2D correlation maps of PglK (Figure 7A) suggests that the dynamic behavior of this exporter is different from that of the importers BtuCD and MalFGK. Unlike the NBDs of the importers, the NBDs of PglK form a completely continuous, single dynamic unit. A similar trend is observed for the TMDs of PglK, which, relative to the TMDs of the importers, form larger and more continuous dynamic units. These observations suggest that, in the exporter, there are fewer hinges and that the motions are more global and rigid. Another prominent mechanistic feature that is revealed by the 2D correlation maps is the long-distance, tight allosteric connection between the substrate-binding "external helix" and the ATP-binding sites (Figures 7A and 7B). Based on structural and functional studies, the external helix directly interacts with the substrate and signals substrate occupancy to the ATP sites. In the subsequent comparison of the three transporters, we equate the external helix to the docking sites of SBPs due to their similar positions, and since both the SBP-docking site and the external helix should relay substrate occupancy to the TMDs and NBDs.

Sequence of Conformational Changes in BtuCD, MalFGK, and PglK

As explained above, using the time-delayed ANM-LD simulations (Figures 5, 6, and S7) and the transfer entropy calculations (Figures S8A and S8B) we can determine which event precedes. We used this approach to determine the kinetic relations between the main functional sites (e.g., ATP sites, coupling helices, gates, and SBP-docking sites, see Figure 8) in BtuCD, MalFGK, and PglK, and compared the sequence of the "signal-transduction" of the allosteric communication in the three transporters.

In BtuCD, binding of ATP is the initiator and main driver of mobility and allosteric communication (Figures 1, 2, 5, S2, S3, and S8A). Its binding triggers the movements of the ATP-binding residues, which is transmitted diagonally to the coupling helix (Figure 8A). The coupling helix subsequently moves, and its movement transmits a signal directly to the BtuF-binding sites that are located above it and also to the cytoplasmic gates of the other BtuC monomer. The movement of the cytoplasmic gates is subsequently transmitted to the BtuF-binding sites of the same BtuC chain. Consequently, the coupling helix drives (directly and indirectly) the movement of the BtuF-binding sites of both chains (Figure 8A).

The sequence and directionality of allosteric conduction is different in MalFGK, with MalE being the main driver of allosteric communication (Figures 6B and 6C). Docking of MalE triggers the rearrangement of the MalE-binding residues, and their movement transmits a signal to the transmembrane maltose-binding site, to the cytoplasmic gates, and to the ATP-binding residues at the NBD (Figure 8B). Consequently, docking of MalE prepares the transmembrane maltose-binding site and signals the cytoplasmic gates and NBDs to close. The movement of the transmembrane maltose-binding residues is then transmitted to the coupling helices, and to the NBDs. The movement of the coupling helices also transmits a signal to the NBDs, which, in turn, report back to the coupling helices on their conformational state (Figure 8B). This feedback of conformational information also takes place at the cytoplasmic gates, which relay their conformational state back to the transmembrane maltose-binding residues.

PglK is different structurally and mechanistically from both importers (Perez et al., 2015), and it is thus of no surprise that it uses a distinct allosteric network. In PglK, the allosteric network seems more intricate and is best described by two nested allosteric cycles, with the allosteric signal propagating between the NBDs and external helices in a cyclic manner.

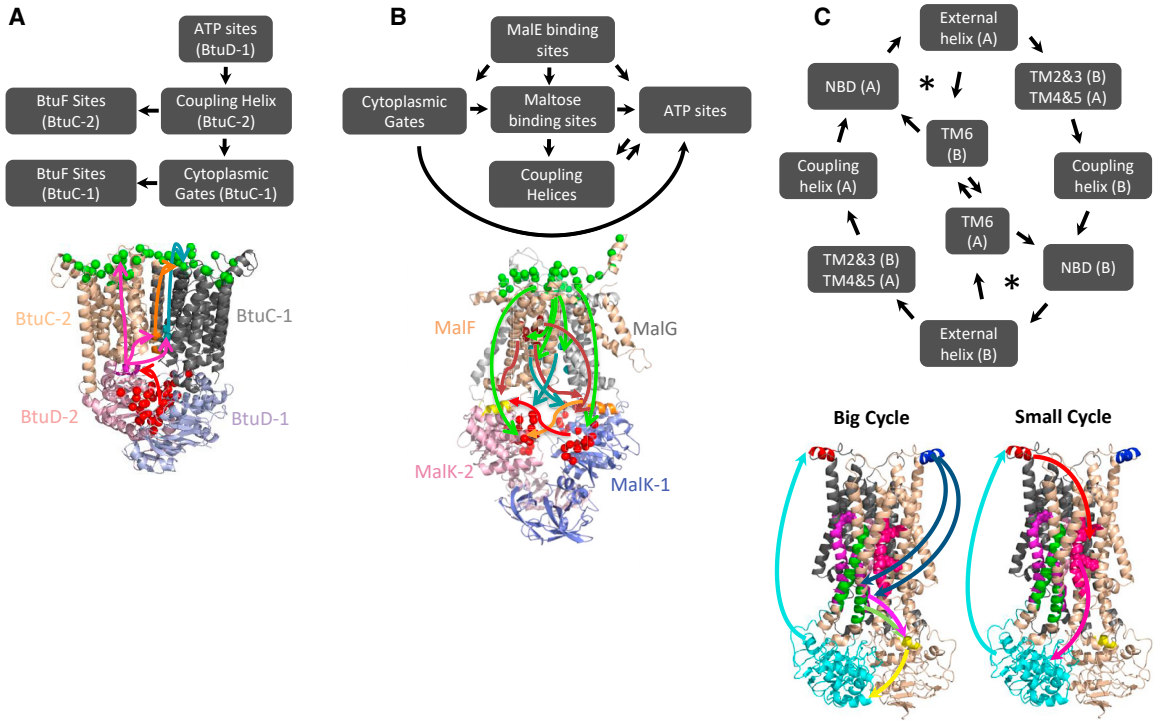

Figure 8. Different Mechanical Transduction Networks and Causality Relations in BtuCD, MalFGK, and PglK

A schematic representation of the origin and the propagation of the allosteric signal in BtuCD (A), MalFGK (B), and PglK (C). Arrows indicate the direction of propagation of the conformational changes, as inferred from the time-delayed simulations. In (A) and (B), spheres indicate residues involved in binding of ATP (red) and docking of the SBP (green). In (C), the external helices are colored red (chain B) and blue (chain A), TM6 in pink, TMs 4 and 5 in green, TMs 2 and 3 in magenta, coupling helix in yellow, and the NBD of chain B in cyan. In (C), the asterisk denotes the "small" allosteric cycle.

In the "big" signaling cycle (Figure 8C), the external helix of chain A drives the movement of TM helices 2–3 of chain B and TM helices 4–5 of chain A. Importantly, these regions harbor the positively charged residues R86 and R260, which have been proposed to interact directly with the substrate (Perez et al., 2015). From these regions, the signal is transmitted to the coupling helix of chain B, and then to the NBDs of chain B. From here, the signal propagates back to the external helix of chain B. From the external helix of chain B, the signal continues as described above for external helix A, via TM2-3 A/TM4-5 B, to coupling helix A, to NBD A, and finally back to external helix A, concluding the external helix-NBD cross-talk of the big allosteric cycle. In the "small" allosteric cycle (Figure 8C), the structural rearrangements of the external helix (chain A) are transmitted to TM6 of chain B. TM6 harbors the positively charged residues R302 and R309, which together with R86 and R260 of TM2-3/TM4-5 participate in substrate recognition. From TM6, the signal is transmitted to the NBD (of chain A) and then back to the external helix of the same chain, concluding the external helix-NBD crosstalk of the small allosteric cycle. This external helix-NBD crosstalk that is present in both allosteric cycles creates an inter-dependence between ATP hydrolysis and substrate binding and release: binding of substrate signals substrate occupancy subsequently modulating ATP binding and release and stimulating ATPase activity. In turn, the nucleotide occupancy of the NBD modulates the binding and release of the substrate, thus controlling the transport process.

DISCUSSION

The exploration of structural dynamics and allosteric networks often requires a combination of computational and experimental approaches. However, the slow rates of transport, ATPase, and conformational changes of ABC transporters (minutes, seconds, and milliseconds, respectively) (Ames et al., 1996; Liu et al., 1997; Tal et al., 2013; Goudsmits et al., 2017; Yang et al., 2018), preclude the use of conventional MD simulations. We therefore developed a novel approach, which is tailored for enhanced sampling of the conformational space of slow reactions. Reassuringly, we observed a good correlation between the results of the ANM-LD simulations and previously published experimental data (Figures 1 and 2) (Davidson et al., 1992; Borths et al., 2005; Orelle et al., 2008; Joseph et al., 2011, 2014; Perez et al., 2015; Yang et al., 2018). Combining GNM with the ANM-LD simulations provided a platform where hinge residues that underlie the allosteric communication can be identified and the effects of point mutations can be evaluated *in silico* (Figure 3). Based on these calculations, we generated 26 point mutations and tested for vitamin B_{12} uptake activity. For 25 out of the 26 mutants, the angular deviation calculations (Figure 3) correctly predicted whether a mutation would abolish transport (Figure 4). Such correlation between computed and experimental results is quite striking, and strongly argues in favor of the usefulness of the ANM-LD method.

The comparison between BtuCD-F and MalFGK-E provided some very interesting insights with respect to their different mechanisms. Previous experimental work demonstrated that MalFGK-E is a substrate-controlled transporter: without maltose, MalE does not efficiently induce the closure of the NBD, and therefore ATP cannot be hydrolyzed (Davidson et al., 1992). This substrate control is achieved at two levels. First, via the large Venus flytrap conformational change that MalE undergoes upon maltose binding (Spurlino et al., 1991; Sharff et al., 1992). This enables the system to sense the presence of substrate. Second, the transmembrane maltose-binding site also participates in substrate occupancy sensing (Khare et al., 2009) and in subsequent control of ATP hydrolysis. These means of substrate control are absent from BtuCD-F: the vitamin B_{12}-free and -bound conformations of BtuF are very similar (Karpowich et al., 2003), and thus cannot report substrate occupancy, and there is no transmembrane-binding site for vitamin B_{12} (Lewinson et al., 2010; Korkhov et al., 2012; Korkhov et al., 2014). These differences between the two transporters are clearly reflected in their respective allosteric network. In MalFGK-E, docking of MalE is the main driver of conformational mobility (Figure 6), and the allosteric signal originates from the MalE-docking site, propagates to the transmembrane maltose-binding site, and onward toward the intracellular to the coupling helices and NBDs (Figure 8B). In MalFGK-E, ATP binding and hydrolysis are the affected party, not the effector. This cause-and-effect relationship is completely reversed in BtuCD-F, where the allosteric signal originates from the NBDs (intracellular) and propagates toward the extracellular to the BtuF-docking sites (Figure 8A). Hence, in MalFGK-E the main allosteric player is the SBP, and in BtuCD-F it is ATP.

PglK, the exporter, presents a more complex allosteric network that combines control by both substrate and ATP. In PglK, the two nested allosteric cycles lead to a crosstalk of causality relations between substrate binding to the external helix and ATP binding to the NBD (Figure 8C). As a result, both ligands play equal roles in controlling the conformational transitions. In a way, PglK uses an allosteric middle ground between MalFKG and BtuCD. Notably, this middle ground behavior of PglK is also mirrored in its ATPase activity: in MalFGK, ATPase activity fully depends on docking of MalE-maltose (Davidson et al., 1992). This control is almost completely absent from BtuCD, which does not require BtuF-vitamin B_{12} for ATP hydrolysis (Tal et al., 2013). In this respect, PglK represents a middle ground between the substrate-dependence of MalFGK and the substrate-independence of BtuCD. Its basal ATPase rates are higher than those of MalFGK yet lower than those of BtuCD, and its substrate-driven stimulation is lower than that of MalFGK yet higher than that of BtuCD (Perez et al., 2015). We find it remarkable that the allosteric fingerprint identified by the ANM-LD simulations captures these mechanistic differences between the systems. We suggest that the dynamic behavior of each system (allosteric connectivity, causality, sequence of events) is embedded in its structure, and propose that these dynamics can be disclosed by mapping the conformational trajectories that lead from one conformation to another.

In the future, as more and more structures of ABC transporters in different conformations become available, we will be able to use simulation and experiments to further study the degree of diversity and speciation of the allosteric networks of ABC transporters.

STAR★METHODS

Detailed methods are provided in the online version of this paper and include the following:

- KEY RESOURCES TABLE
- LEAD CONTACT AND MATERIALS AVAILABILITY
- EXPERRIMENTAL MODELS AND SUBJECT DETAILS
  - Bacterial Strains and Plasmids
- METHODS DETAILS
  - Simulations
  - ANM-LD Simulation Protocol
  - Evaluation of ANM–LD
  - Restricted ANM-LD Simulations
  - Determination of Target Mutation
  - Assessing Mutation Effects In Silico
  - Time-Independent and Time-Delayed Correlations
  - GNM Transfer Entropy
  - Visualization
  - Vitamin B_{12} Utilization Assays
- QUANTIFICATION AND STATISTICAL ANALYSIS
- DATA AND CODE AVAILABLITY

SUPPLEMENTAL INFORMATION

Supplemental Information can be found online at https://doi.org/10.1016/j.str.2020.03.014.

ACKNOWLEDGMENTS

This work was supported by grants from NATO Science for Peace and Security Program (SPS project G4622, to O.L., T.H., and N.B.-T.), the Israeli Academy of Sciences project 1006/18 (to O.L. and J.R.), the United States-Israel Binational Science Foundation (BSF) project 2015102 (to O.L. and J.R.), TÜBITAK (The Scientific and Technological Research Council of Turkey) under grant no. 115M418 (to T.H., B.A., and B.A.F.), Boğaziçi University Research Fund BAP project no. 11160 (to T.H., B.A., and B.A.F.), and the Rappaport Family Institute for biomedical research (to O.L. and J.R.).

AUTHOR CONTRIBUTIONS

Methodology development, molecular simulations, and data analysis, B.A.; functional assays and data analysis, J.R.; methodology development and molecular simulations, B.A.F.; supervision, data analysis, and funds acquisition, N.B.-T.; methodology development, supervision, data analysis, and funds acquisition, T.H.; conceptualization, supervision, data analysis, funds acquisition, and manuscript writing, O.L. All authors participated in manuscript editing.

DECLARATION OF INTERESTS

The authors declare that they have no conflict of interest.

Received: December 16, 2019
Revised: February 20, 2020
Accepted: March 27, 2020
Published: April 21, 2020

REFERENCES

Aittoniemi, J., de Wet, H., Ashcroft, F.M., and Sansom, M.S. (2010). Asymmetric switching in a homodimeric ABC transporter: a simulation study. PLoS Comput. Biol. https://doi.org/10.1371/journal.pcbi.1000762.

Ames, G.F., Liu, C.E., Joshi, A.K., and Nikaido, K. (1996). Liganded and unliganded receptors interact with equal affinity with the membrane complex of

periplasmic permeases, a subfamily of traffic ATPases. J. Biol. Chem. *271*, 14264–14270. http://www.ncbi.nlm.nih.gov/pubmed/8662800.

Atilgan, A.R., Durell, S.R., Jernigan, R.L., Demirel, M.C., Keskin, O., and Bahar, I. (2001). Anisotropy of fluctuation dynamics of proteins with an elastic network model. Biophys. J. *80*, 505–515.

Bahar, I., Atilgan, A.R., and Erman, B. (1997). Direct evaluation of thermal fluctuations in proteins using a single-parameter harmonic potential. Fold. Des. *2*, 173–181.

ter Beek, J., Guskov, A., and Slotboom, D.J. (2014). Structural diversity of ABC transporters. J. Gen. Physiol. *143*, 419–435.

Berens, P. (2009). CircStat: a MATLAB toolbox for circular statistics. J. Stat. Softw. *31*, 1–21.

Bernardi, R.C., Melo, M.C.R., and Schulten, K. (2015). Enhanced sampling techniques in molecular dynamics simulations of biological systems. Biochim. Biophys. Acta *1850*, 872–877.

Berntsson, R.P.-A., Smits, S.H., Schmitt, L., Slotboom, D.J., and Poolman, B. (2010). A structural classification of substrate-binding proteins. FEBS Lett. *584*, 2606–2617.

Borths, E.L., Poolman, B., Hvorup, R.N., Locher, K.P., and Rees, D.C. (2005). In vitro functional characterization of BtuCD-F, the *Escherichia coli* ABC transporter for vitamin B12 uptake. Biochemistry *44*, 16301–16309.

Brünger, A., Brooks, C.L., and Karplus, M. (1984). Stochastic boundary conditions for molecular dynamics simulations of ST2 water. Chem. Phys. Lett. *105*, 495–500.

Cadieux, N., Bradbeer, C., Reeger-Schneider, E., Köster, W., Mohanty, A.K., Wiener, M.C., and Kadner, R.J. (2002). Identification of the periplasmic cobalamin-binding protein BtuF of *Escherichia coli*. J. Bacteriol. *184*, 706–717.

Cui, Q., and Bahar, I. (2006). Normal Mode Analysis: Theory and Applications to Biological and Chemical Systems (Chapman & Hall/CRC). https://www.crcpress.com/Normal-Mode-Analysis-Theory-and-Applications-to-Biological-and-Chemical/Cui-Bahar/p/book/9781584884729.

Case, D.A., Darden, T.A., Cheatham, T.E., Simmerling, C.L., III, Wang, J., Duke, R.E., Luo, R., Walker, R.C., Zhang, W., Merz, K.M., et al. (2010). AMBER 11 (University of California). http://ambermd.org/.

Dassa, E., and Bouige, E. (2001). The ABC of ABCs: a phylogenetic and functional classification of ABC systems in living organisms. Res. Microbiol. *152*, 211–229.

Davidson, A.L., Shuman, H.A., and Nikaido, H. (1992). Mechanism of maltose transport in *Escherichia coli*: transmembrane signaling by periplasmic binding proteins. Proc. Natl. Acad. Sci. U S A *89*, 2360–2364. http://www.ncbi.nlm.nih.gov/pubmed/1549599.

Dokholyan, N.V. (2016). Controlling allosteric networks in proteins. Chem. Rev. *116*, 6463–6487.

Eddy, S.R. (1998). Profile hidden Markov models. Bioinformatics *14*, 755–763. http://www.ncbi.nlm.nih.gov/pubmed/9918945.

Fiser, A., Do, R.K., and Sali, A. (2000). Modeling of loops in protein structures. Protein Sci. *9*, 1753–1773.

Fiser, A., and Sali, A. (2003). ModLoop: automated modeling of loops in protein structures. Bioinformatics *19*, 2500–2501.

Fulyani, F., Schuurman-Wolters, G.K., Zagar, A.V., Guskov, A., Slotboom, D.J., and Poolman, B. (2013). Functional diversity of tandem substrate-binding domains in ABC transporters from pathogenic bacteria. Structure *21*, 1879–1888.

Glaser, F., Pupko, T., Paz, I., Bell, R.E., Bechor-Shental, D., Martz, E., and Ben-Tal, N. (2003). ConSurf: identification of functional regions in proteins by surface-mapping of phylogenetic information. Bioinformatics *19*, 163–164. http://www.ncbi.nlm.nih.gov/pubmed/12499312.

Gottesman, M.M., Fojo, T., and Bates, S.E. (2002). Multidrug resistance in cancer: role of ATP-dependent transporters. Nat. Rev. Cancer *2*, 48–58.

Goudsmits, J.M.H., Slotboom, D.J., and van Oijen, A.M. (2017). Single-molecule visualization of conformational changes and substrate transport in the vitamin B12 ABC importer BtuCD-F. Nat. Commun. *8*, 1652.

Hacisuleyman, A., and Erman, B. (2017). Causality, transfer entropy, and allosteric communication landscapes in proteins with harmonic interactions. Proteins *85*, 1056–1064.

Haliloglu, T., Bahar, I., and Erman, B. (1997). Gaussian dynamics of folded proteins. Phys. Rev. Lett. *79*, 3090–3093.

van der Heide, T., and Poolman, B. (2000). Osmoregulated ABC-transport system of *Lactococcus lactis* senses water stress via changes in the physical state of the membrane. Proc. Natl. Acad. Sci. U S A *97*, 7102–7106. http://www.ncbi.nlm.nih.gov/pubmed/10860977.

Higgins, C.F. (1992). ABC transporters: from microorganisms to man. Annu. Rev. Cell Biol. *8*, 67–113. http://www.ncbi.nlm.nih.gov/entrez/query.fcgi?cmd=Retrieve&db=PubMed&dopt=Citation&list_uids=1282354.

Holland, I.B., Cole, S.P.C., Kuchler, K., and Higgins, C.F. (2003). ABC Proteins: From Bacteria to Man (Academic Press).

Hvorup, R.N., Goetz, B.A., Niederer, M., Hollenstein, K., Perozo, E., and Locher, K.P. (2007). Asymmetry in the structure of the ABC transporter-binding protein complex BtuCD-BtuF. Science *317*, 1387–1390.

Johnson, Z.L., and Chen, J. (2018). ATP binding enables substrate release from multidrug resistance protein 1. Cell *172*, 81–89.e10.

Jones, P.M., and George, A.M. (2002). Mechanism of ABC transporters: a molecular dynamics simulation of a well characterized nucleotide-binding subunit. Proc. Natl. Acad. Sci. U S A *99*, 12639–12644.

Joseph, B., Jeschke, G., Goetz, B.A., Locher, K.P., and Bordignon, E. (2011). Transmembrane gate movements in the type II ATP-binding cassette (ABC) importer BtuCD-F during nucleotide cycle. J. Biol. Chem. *286*, 41008–41017.

Joseph, B., Korkhov, V.M., Yulikov, M., Jeschke, G., and Bordignon, E. (2014). Conformational cycle of the vitamin B12 ABC importer in liposomes detected by double electron-electron resonance (DEER). J. Biol. Chem. *289*, 3176–3185.

Karpowich, N.K., Huang, H.H., Smith, P.C., and Hunt, J.F. (2003). Crystal structures of the BtuF periplasmic-binding protein for vitamin B12 suggest a functionally important reduction in protein mobility upon ligand binding. J. Biol. Chem. *278*, 8429–8434.

Khare, D., Oldham, M.L., Orelle, C., Davidson, A.L., and Chen, J. (2009). Alternating access in maltose transporter mediated by rigid-body rotations. Mol. Cell *33*, 528–533.

Kim, Y., and Chen, J. (2018). Molecular structure of human P-glycoprotein in the ATP-bound, outward-facing conformation. Science *359*, 915–919.

Korkhov, V.M., Mireku, S.A., Veprintsev, D.B., and Locher, K.P. (2014). Structure of AMP-PNP-bound BtuCD and mechanism of ATP-powered vitamin B12 transport by BtuCD-F. Nat. Struct. Mol. Biol. *21*, 1097–1099.

Korkhov, V.M., Mireku, S.A., and Locher, K.P. (2012). Structure of AMP-PNP-bound vitamin B12 transporter BtuCD-F. Nature *490*, 367–372.

Lanfermeijer, F.C., Picon, A., Konings, W.N., and Poolman, B. (1999). Kinetics and consequences of binding of nona- and dodecapeptides to the oligopeptide binding protein (OppA) of *Lactococcus lactis*. Biochemistry *38*, 14440–14450.

Lewinson, O., Lee, A.T., Locher, K.P., and Rees, D.C. (2010). A distinct mechanism for the ABC transporter BtuCD-F revealed by the dynamics of complex formation. Nat. Struct. Mol. Biol. *17*, 332–338.

Lewinson, O., and Livnat-Levanon, N. (2017). Mechanism of action of ABC importers: conservation, divergence, and physiological adaptations. J. Mol. Biol. https://doi.org/10.1016/j.jmb.2017.01.010.

Liu, C.E., Liu, P.Q., and Ames, G.F. (1997). Characterization of the adenosine triphosphatase activity of the periplasmic histidine permease, a traffic ATPase (ABC transporter). J. Biol. Chem. *272*, 21883–21891. http://www.ncbi.nlm.nih.gov/pubmed/9268321.

Locher, K.P., Lee, A.T., and Rees, D.C. (2002). The *E. coli* BtuCD structure: a framework for ABC transporter architecture and mechanism. Science *10*, 1091–1098.

Locher, K.P. (2016). Mechanistic diversity in ATP-binding cassette (ABC) transporters. Nat. Struct. Mol. Biol. *23*, 487–493.

MathWorks. (2019). MathWorks Announces Release 2019b of MATLAB and Simulink - MATLAB & Simulink. https://www.mathworks.com/company/newsroom/mathworks-announces-release-r2019b-of-matlab-and-simulink.html.

Maximova, T., Moffatt, R., Ma, B., Nussinov, R., and Shehu, A. (2016). Principles and overview of sampling methods for modeling macromolecular structure and dynamics. PLoS Comput. Biol. *12*, e1004619.

Mayrose, I., Graur, D., Ben-Tal, N., and Pupko, T. (2004). Comparison of site-specific rate-inference methods for protein sequences: empirical Bayesian methods are superior. Mol. Biol. Evol. *21*, 1781–1791.

McDevitt, C.A., Ogunniyi, A.D., Valkov, E., Lawrence, M.C., Kobe, B., McEwan, A.G., and Paton, J.C. (2011). A molecular mechanism for bacterial susceptibility to zinc. PLoS Pathog. *7*, e1002357.

Montanucci, L., Martelli, P.L., Ben-Tal, N., and Fariselli, P. (2019). A natural upper bound to the accuracy of predicting protein stability changes upon mutations. Bioinformatics *35*, 1513–1517.

Nguyen, P.T., Lai, J.Y., Lee, A.T., Kaiser, J.T., and Rees, D.C. (2018). Noncanonical role for the binding protein in substrate uptake by the MetNI methionine ATP binding cassette (ABC) transporter. Proc. Natl. Acad. Sci. U S A *115*, E10596–E10604.

Oldham, M.L., Khare, D., Quiocho, F.A., Davidson, A.L., and Chen, J. (2007). Crystal structure of a catalytic intermediate of the maltose transporter. Nature *450*, 515–521.

Oldham, M.L., and Chen, J. (2011). Snapshots of the maltose transporter during ATP hydrolysis. Proc. Natl. Acad. Sci. U S A *108*, 15152–15156.

Oliveira, A.S.F., Baptista, A.M., and Soares, C.M. (2011). Inter-domain communication mechanisms in an ABC importer: a molecular dynamics study of the MalFGK2E complex. PLoS Comput. Biol. *7*, e1002128.

Oloo, E.O., and Tieleman, D.P. (2004). Conformational transitions induced by the binding of MgATP to the vitamin B12 ATP-binding cassette (ABC) transporter BtuCD. J. Biol. Chem. *279*, 45013–45019.

Orelle, C., Ayvaz, T., Everly, R.M., Klug, C.S., and Davidson, A.L. (2008). Both maltose-binding protein and ATP are required for nucleotide-binding domain closure in the intact maltose ABC transporter. Proc. Natl. Acad. Sci. U S A *105*, 12837–12842.

Perez, C., Gerber, S., Boilevin, J., Bucher, M., Darbre, T., Aebi, M., Reymond, J.L., and Locher, K.P. (2015). Structure and mechanism of an active lipid-linked oligosaccharide flippase. Nature *524*, 433–438.

Pinkett, H.W., Lee, A.T., Lum, P., Locher, K.P., and Rees, D.C. (2007). An inward-facing conformation of a putative metal-chelate-type ABC transporter. Science *315*, 373–377.

Proctor, E.A., Kota, P., Aleksandrov, A.A., He, L., Riordan, J.R., and Dokholyan, N.V. (2015). Rational coupled dynamics network manipulation rescues disease-relevant mutant cystic fibrosis transmembrane conductance regulator. Chem. Sci. *6*, 1237–1246.

Qasem-Abdullah, H., Perach, M., Livnat-Levanon, N., and Lewinson, O. (2017). ATP binding and hydrolysis disrupt the high-affinity interaction between the heme ABC transporter HmuUV and its cognate substrate-binding protein. J. Biol. Chem. *292*, 14617–14624.

Quiocho, F.A., Spurlino, J.C., and Rodseth, L.E. (1997). Extensive features of tight oligosaccharide binding revealed in high-resolution structures of the maltodextrin transport/chemosensory receptor. Structure *5*, 997–1015.

Remy, L., Carrière, M., Derré-Bobillot, A., Martini, C., Sanguinetti, M., and Borezée-Durant, E. (2013). The *Staphylococcus aureus* Opp1 ABC transporter imports nickel and cobalt in zinc-depleted conditions and contributes to virulence. Mol. Microbiol. *87*, 730–743.

Riordan, J.R. (2008). CFTR function and prospects for therapy. Annu. Rev. Biochem. *77*, 701–726.

Schymkowitz, J., Borg, J., Stricher, F., Nys, R., Rousseau, F., and Serrano, L. (2005). The FoldX web server: an online force field. Nucleic Acids Res. *33* (Web Server), W382–W388.

Sebulsky, M.T., Shilton, B.H., Speziali, C.D., and Heinrichs, D.E. (2003). The role of FhuD2 in iron(III)-hydroxamate transport in *Staphylococcus aureus*. Demonstration that FhuD2 binds iron(III)-hydroxamates but with minimal conformational change and implication of mutations on transport. J. Biol. Chem. *278*, 49890–49900.

Sharff, A.J., Rodseth, L.E., Spurlino, J.C., and Quiocho, F.A. (1992). Crystallographic evidence of a large ligand-induced hinge-twist motion between the two domains of the maltodextrin binding protein involved in active transport and chemotaxis. Biochemistry *31*, 10657–10663. http://www.ncbi.nlm.nih.gov/pubmed/1420181.

Spurlino, J.C., Lu, G.Y., and Quiocho, F.A. (1991). The 2.3-A resolution structure of the maltose- or maltodextrin-binding protein, a primary receptor of bacterial active transport and chemotaxis. J. Biol. Chem. *266*, 5202–5219. http://www.ncbi.nlm.nih.gov/pubmed/2002054.

Tal, N., Ovcharenko, E., and Lewinson, O. (2013). A single intact ATPase site of the ABC transporter BtuCD drives 5% transport activity yet supports full in vivo vitamin B12 utilization. Proc. Natl. Acad. Sci. U S A *110*, 5434–5439.

Tanaka, K.J., Song, S., Mason, K., and Pinkett, H.W. (2018). Selective substrate uptake: the role of ATP-binding cassette (ABC) importers in pathogenesis. Biochim. Biophys. Acta Biomembr. *1860*, 868–877.

Thomas, C., and Tampé, R. (2018). Multifaceted structures and mechanisms of ABC transport systems in health and disease. Curr. Opin. Struct. Biol. *51*, 116–128.

Vigonsky, E., Ovcharenko, E., and Lewinson, O. (2013). Two molybdate/tungstate ABC transporters that interact very differently with their substrate binding proteins. Proc. Natl. Acad. Sci. U S A *110*, 5440–5445.

Wodak, S.J., Paci, E., Dokholyan, N.V., Berezovsky, I.N., Horovitz, A., Li, J., Hilser, V.J., Bahar, I., Karanicolas, J., Stock, G., et al. (2019). Allostery in its many disguises: from theory to applications. Structure *27*, 566–578.

Worth, C.L., Preissner, R., and Blundell, T.L. (2011). SDM—a server for predicting effects of mutations on protein stability and malfunction. Nucleic Acids Res. *39* (suppl), W215–W222.

Yang, M., Livnat Levanon, N., Acar, B., Aykac Fas, B., Masrati, G., Rose, J., Ben-Tal, N., Haliloglu, T., Zhao, Y., and Lewinson, O. (2018). Single-molecule probing of the conformational homogeneity of the ABC transporter BtuCD. Nat. Chem. Biol. *14*, 715–722.

Yin, S., Ding, F., and Dokholyan, N.V. (2007). Modeling backbone flexibility improves protein stability estimation. Structure *15*, 1567–1576.

STAR★METHODS

KEY RESOURCES TABLE

REAGENT or RESOURCE	SOURCE	IDENTIFIER
Antibodies		
Monoclonal Anti-polyHistidine–Peroxidase antibody	Sigma-Aldrich	Cat# A7058; RRID: AB_258326
Bacterial and Virus Strains		
DH5α	Invitrogen	N/A
BL21-Gold (DE3)	Stratagene	N/A
wild-type BW25113, Δ*metE::kan* from the Keio collection and Δ*metE* Δ*btuD::kan* and Δ*metE* Δ*btuC::kan*	Lewinson lab	N/A
Chemicals, Peptides, and Recombinant Proteins		
Vitamin B_{12}	Sigma	47869
L-Methionine	Sigma	M9625
Critical Commercial Assays		
QuikChange™ Lightning	Stratagene	N/A
Deposited Data		
BtuCD	(Locher et al., 2002)	PDB ID 1L7V
BtuCD	(Korkhov et al., 2014)	PDB ID 4R9U
BtuCD	(Korkhov et al., 2012)	PDB ID 4FI3
BtuCD	(Hvorup et al., 2007)	PDB ID 2QI9
MalFGK	(Pinkett et al., 2007)	PDB ID 3PUY
MalFGK	(Khare et al., 2009).	PDB ID 3FH6
PglK	(Perez et al., 2015),	PDB ID 5C78
PglK	(Perez et al., 2015).	PDB ID 5C73
Oligonucleotides		
See Table S1	This study	N/A
Recombinant DNA		
$pBtuC_2D_2$ is a pET-21b(+) (Novagen) derivative encodes His tag BtuC and BtuD.	Douglas Rees lab, Caltech	N/A
$pBtuC_2D_2$ G244R	This study	N/A
$pBtuC_2D_2$ L90R	This study	N/A
$pBtuC_2D_2$ L172G	This study	N/A
$pBtuC_2D_2$ L172A	This study	N/A
$pBtuC_2D_2$ A121W	This study	N/A
$pBtuC_2D_2$ I186W	This study	N/A
$pBtuC_2D_2$ A121I	This study	N/A
$pBtuC_2D_2$ A121R	This study	N/A
$pBtuC_2D_2$ R232W	This study	N/A
$pBtuC_2D_2$ D291W	This study	N/A
$pBtuC_2D_2$ A121L	This study	N/A
$pBtuC_2D_2$ G124W	This study	N/A
$pBtuC_2D_2$ G67S	This study	N/A
$pBtuC_2D_2$ A121C	This study	N/A
$pBtuC_2D_2$ A121G	This study	N/A
$pBtuC_2D_2$ A121T	This study	N/A
$pBtuC_2D_2$ A121V	This study	N/A
$pBtuC_2D_2$ A121H	This study	N/A

(*Continued on next page*)

Continued

REAGENT or RESOURCE	SOURCE	IDENTIFIER
pBtuC$_2$D$_2$ G244D	This study	N/A
pBtuC$_2$D$_2$ G244A	This study	N/A
pBtuC$_2$D$_2$ M211F	This study	N/A
pBtuC$_2$D$_2$ L90G	This study	N/A
pBtuC$_2$D$_2$ G48R	This study	N/A
pBtuC$_2$D$_2$ E27R	This study	N/A
pBtuC$_2$D$_2$ G67W	This study	N/A
pBtuC$_2$D$_2$ G54W	This study	N/A
pBtuC$_2$D$_2$ C279F	This study	N/A
pBtuC$_2$D$_2$ A200H	This study	N/A
Software and Algorithms		
AMN-LD	This study	https://github.com/prclab/anmld_mutant
Amber 11- Sander	(Case et al., 2010)	N/A
PyMOL	The PyMOL Molecular Graphics System, Version 1.3, Schrodingr, LLC.	N/A
MATLAB	(MathWorks, 2019; Berens, 2009)	N/A

LEAD CONTACT AND MATERIALS AVAILABILITY

Further information and requests for resources and reagents should be directed to and will be fulfilled by the Lead Contact, Oded Lewinson (lewinson@technion.ac.il).

All unique reagents generated in this study are available from Lead contact with a completed Materials Transfer Agreement.

EXPERRIMENTAL MODELS AND SUBJECT DETAILS

Bacterial Strains and Plasmids

No animal or human studies were conducted in this research.

DH5α (Invitrogen) was used for all cloning procedures, and BL21-Gold (DE3) (Stratagene) was the host for protein expression. For vitamin B_{12} utilization assays, we used the wild-type strain BW25113 and its isogenic deletion mutants, Δ*metE::kan* from the Keio collection and Δ*metE* Δ*btuD::kan* and Δ*metE* Δ*btuC::kan* strains generated in our lab. Site-directed mutagenesis was performed using a commercial kit (QuikChange™ Lightning, Stratagene). The correct insertion of all mutations (and lack of additional undesired mutations) was verified by sequencing.

Unless mentioned otherwise, bacteria strains were grown in LB medium.

METHODS DETAILS

Simulations

To explore the conformational transition pathways connecting functional states of BtuCD, MalFGK and PglK, we designed a hybrid molecular simulation methodology, ANM–LD, which integrates a low-resolution α-carbon-based anisotropic network model (ANM) with stochastic all-atom implicit solvent Langevin dynamics (LD) simulations. ANM–LD utilizes the structure's intrinsic dynamics to guide functional conformational changes through cycles of perturbations of the system in its dynamic (ANM) modes toward a target conformation, followed by short time LD simulations. The time window in ANM–LD simulations does not reflect the real time of the simulated transitions, yet provides information on the transition mechanism and the order of events that cannot be achieved with current computational methods such as molecular dynamics (MD) simulations. Moreover, having accessible internal dynamics as the only bias toward the target conformation enables the determination of physical and biological transition pathways.

ANM-LD requires that the initial and target conformations contain the exact same number of interaction sites. Therefore, to simulate the conformational transition between the apo and holo states the ligands were removed from the PDB files of the latter, without any effect on the holo conformation itself. Using the crystal structures of the ligand-bound states as the target conformations ensures that the conformational trajectory leads to the holo state, implicitly accounting for the effect of the ligand.

For BtuCD, starting from the APO state (PDB ID 1L7V) (Locher et al., 2002), ANM-LD simulations were performed toward the ATP-bound structure (PDB ID 4R9U) (Korkhov et al., 2014), the ATP/BtuF-bound structure (PDB ID 4FI3) (Korkhov et al., 2012) and the BtuF-bound structure (PDB ID 2QI9) (Hvorup et al., 2007). Additionally, ANM-LD simulations was also run with the ATP-bound structure as the initial state toward the ATP/BtuF-bound conformation.

For MalFGK$_2$, we simulated the forward and reverse transitions from the APO state (PDB ID 3PUY) (Pinkett et al., 2007) to the ATP/MalE bound conformation (PDB ID 3FH6) (Khare et al., 2009); and for PglK, the forward and reverse transitions from the APO (PDB ID 5C78) (Perez et al., 2015) to the ADP-bound (PDB ID 5C73) (Perez et al., 2015) conformations.

Since utilization of ANM-LD requires that the initial and target conformations include the same atoms, the nucleotides and substrate binding proteins were not considered in the simulations. For MalFGK, the periplasmic part of Chain F (S113-K262) was also removed in the MalE + ATP bound state in order to equalize residue numbers of this state with the APO state which do not contain this region. The missing residues between the initial and target conformations were modeled by the ModWeb/ModLoop servers (Fiser et al., 2000; Fiser and Sali, 2003) and potential steric clashes were removed by Chiron 7.

For BtuCD, starting from RMSDs of up to 3.7 Å between the initial and target conformations, the RMSD between the final conformation (of the simulation) and the target conformation were in the range of 1.0 Å-1.5 Å. For MalFGK, starting from a 6.9 Å RMSD between the initial and target conformation, the RMSD between the final conformations approached to within 2.7 Å of the target conformation. For PglK, the RMSD between the final conformation of the simulation and the target conformation were within 3.1 Å, starting from RMSDs of 16.7 Å between the initial and target conformations.

ANM-LD Simulation Protocol

In the hybrid framework of ANM-LD, an in-house program (https://github.com/prclab/anmld_mutant) is used for the ANM calculations and consecutive call-outs of energy minimization and LD simulation steps performed in Amber 11-Sander (Case et al., 2010) biomolecular simulation package. With given initial structure, ANM–LD constructs the Hessian matrix (H) of the second derivative of the intramolecular potential function (V) for the current initial structure at each iteration cycle by setting a distance threshold radius (R_{cut} = 13 A) to define the neighbor interactions between α-carbon atoms. Using the γ force constant and $\Delta\mathbf{R}$ fluctuation vectors, potential energy is defined in ANM as:

$$V = (\gamma/2)\ \Delta\mathbf{R}^T\ \mathbf{H}\Delta\mathbf{R} \qquad \text{(Equation 1)}$$

The pseudoinverse of the Hessian matrix reveals 3N-6 intrinsic modes of motion according to the following equation of correlation between fluctuations of residue i and j (Atilgan et al., 2001)

$$<\Delta\mathbf{R}_i.\Delta\mathbf{R}_j> = (3k_BT/\gamma)\ tr\ [\mathbf{H}^{-1}] = (3k_BT/\gamma)\ \Sigma_k\ tr[\lambda_k^{-1}\ \mathbf{U}_k\ \mathbf{U}^T{}_k\ ]_{ij} \qquad \text{(Equation 2)}$$

λ_k is k_{th} eigenvalue and $\mathbf{U}_k$ is kth eigenvector of **H** representing kth mode of motion, k_B is the Boltzmann constant and T is the absolute temperature in degrees Kelvin.

By the application of a deformation factor (DF = 0.2-1 A), an orthogonal transformation of the system is done in the ANM mode that overlaps most with the difference vector between the structurally aligned initial conformation of the current cycle and the target conformation. DF deforms the structure along $\boldsymbol{U}_{best}$, the ANM mode that best overlaps with the positional difference vector between the initial and target conformations. The energy of this conformation is minimized for 500 steps (steepest descent for the first 50 steps and then conjugate gradient for the rest; using the Amber 11-Sander 4 biomolecular simulation program), resulting in positional changes $\Delta\boldsymbol{R}_{\boldsymbol{Eng.Min}}$. This is followed by 100 steps of LD simulation with a time step of 0.2 fs (20 fs = 100 steps × 0.2 fs) at temperature T = 310 K with a damping constant of γ = 5 ps−1, leading to further structural relaxation with conformational changes of $\Delta\boldsymbol{R}_{\boldsymbol{LD}}$. The intermediate conformation obtained undergoes another cycle of ANM and LD, and more iteration follow until convergence, i.e., when the system gets close enough to the goal conformation or when the changes become too small (Case et al., 2010).

A simplified equation of positional sampling in each ANM-LD cycle is given below as

$$\boldsymbol{R}_{\boldsymbol{new}} = \boldsymbol{R}_{\boldsymbol{old}} + \Delta\boldsymbol{R}_{\boldsymbol{ANM}} + \Delta\boldsymbol{R}_{\boldsymbol{Eng.Min.}} + \Delta\boldsymbol{R}_{\boldsymbol{LD}} \qquad \text{(Equation 3)}$$

in which

$$\Delta\boldsymbol{R}_{\boldsymbol{ANM}} = \boldsymbol{U}_{\boldsymbol{best}}DF \qquad \text{(Equation 4)}$$

The ANM and LD steps are iteratively performed until the RMSD between the final and target conformations reaches a plateau. Each of these steps represents an intermediate conformations along the transition pathway from the initial to target conformations.

Evaluation of ANM–LD

ANM–LD simulations were run for a diverse data set of proteins including globular and non-globular proteins. These include Adenylate Kinase (AdK), membrane proteins such as FimD and ClyA (B.A.F, B.A., and T.H., unpublished data), and the ABC transporters of the present study. Starting with RMSDs of 14 to 24 Å between the initial and target conformation (depending on the system studied), the target conformation was approached to within an RMSD of 1.4-3.1 Å. Importantly, the transition pathway between the open and closed states of Adenylate Kinase (AdK), as determined by ANM-LD, included the known structures of homologous proteins, even though these were not used to guide the simulation (B.A.F., B.A., and T.H., unpublished data). This observation strongly supports the utility of ANM-LD in identifying conformational trajectories that are biologically and physically relevant.

Restricted ANM-LD Simulations

ANM-LD simulations are able to identify intrinsic modes of motion that are key for a given conformational transition. To evaluate the contribution of a specific mode of motion to the conformational transition, a *restricted* ANM-LD simulation protocol was utilized. In this restricted protocol, a specific ANM mode (or set of modes) are disallowed. In other words, in a *restricted* ANM-LD simulation a mode of motion of interest is blocked, and the effects of this blocking on the dynamics of the transition are evaluated. Such restrictions may lead to alternative pathways of conformational transitions, and in the case of an irreplaceable mode of motion, a particular restriction will impede the conformational transition.

Determination of Target Mutation

In ANM-LD, the modes of motion chosen by the algorithm in the early cycles of the simulation encompass highly collective and cooperative modes of motion (termed ''slow modes'') that are responsible for global conformational changes. Of the ten ''slow-modes'' that are intrinsic to APO BtuCD, four such highly-collective ''slow-modes'' were most frequently selected in the majority of the simulations. These four modes were thus considered to be major dynamic components of the transitions toward the ATP-bound and BtuF + ATP-bound conformations. When these modes were blocked in *restricted* simulations (see above), the conformational transition pathway was altered and key functional sites (cytoplasmic and periplasmic gates, BtuF docking sites) displayed an abnormal dynamic behavior. To identify key hinge residues that enable the fundamental motions of BtuCD, these four most-frequently used ANM modes were mapped onto a 1-D dynamic space defined by Gaussian Network Model (Bahar et al., 1997; Haliloglu et al., 1997) (GNM) based on their similarity to GNM mode shapes. In GNM, the Kirchhoff matrix Γ replaces the Hessian matrix (H) of ANM (Equation 1), and the correlation between ΔR_i and ΔR_j is decomposed into N-1 modes by the following equation.

$$< \Delta \mathbf{R}_i \,.\, \Delta \mathbf{R}_j > = (3k_B T/\gamma)\,[\mathbf{\Gamma}^{-1}]_{ij} = (3k_B T/\gamma)\,\Sigma_k\,[\lambda_k^{-1}\,\mathbf{U}_k\,\mathbf{U}^T{}_k\,]_{ij} \qquad \text{(Equation 5)}$$

Minima points of mean square fluctuations at a given GNM mode k are defined as the hinge residues.

Of the hinge residues identified by this GNM-ANM-LD analysis, we focused on ones that are evolutionarily conserved. To scale the conservation of the hinge residues we conducted independent ConSurf (Glaser et al., 2003) calculations with BtuCD (PDB ID 1L7V, subunit A). Homologues with 35% to 95% sequence identity were collected using HMMER (Eddy, 1998) with one iteration and an E-value of 0.0001 against the clean UniProt database. 300 unique sequences were retrieved, and multiply aligned using MAFFT-L-INS-i. The rate of evolution at each site was calculated using the Bayesian method (Mayrose et al., 2004) and the LG evolutionary model. For mutational analysis, we chose hinge residues that displayed the highest ConSurf conservation score (8 or 9 on a 1-9 scale).

Assessing Mutation Effects In Silico

In silico mutations were generated with Pymol 1.3 (The PyMOL Molecular Graphics System, Version 1.3, Schrodingr, LLC.) in APO and in ATP&BtuF-bound BtuCD. The mutant structures were then energy minimized using the Amber 11-Sander biomolecular simulation package (Case et al., 2010), and the resulting initial and final conformations were used to perform ANM-LD simulations.

The mutant ANM-LD transition pathways were then assessed with respect to the sampled bond/backbone rotation angles (ϕ) of hinge residues (and their contact residues, Figures S4B and S3) that enable the movement performed by the ANM-1 mode of motion. ANM-1 was the most frequently used mode of motion in the transition from the APO to ATP & BtuF bound conformations of BtuCD. To quantify a mutant's deviation (from WT), a cumulative angular deviation score (AD) was calculated (Equation 6) as the sum of absolute differences between the mutant and mean WT (μ_{WT}) angles over each frame and each hinge of ANM-1 (and their immediate neighbors in either sequence or 3D space).

$$AD(mutant) = \sum_{\substack{ANM-1 \\ hinge\ res}} \sum_{frames} |(\varphi_{mutant}(resno, frame) - \mu_{WT}(resno, frame))| \qquad \text{(Equation 6)}$$

Large AD scores indicate that the mutation caused a larger perturbation.

Time-Independent and Time-Delayed Correlations

Positional fluctuation vectors ($\Delta\mathbf{R}$) of residues i and j were calculated as deviations of the current position of their α-carbon atoms from the corresponding mean position. Mean positions were determined in a given time window of the transition pathway in ANM-LD steps.

Dynamical cross correlations between the fluctuations of residues i ($\Delta\mathbf{R}_i$) and j ($\Delta\mathbf{R}_j$) were calculated as

$$C_{ij}(\tau) = \frac{\langle \Delta \boldsymbol{R}i(t)\Delta \boldsymbol{R}j(t+\tau)\rangle}{\sqrt{\langle \Delta \boldsymbol{R}i(t)^2\rangle}\sqrt{\langle \Delta \boldsymbol{R}j(t+\tau)^2\rangle}} \qquad \text{(Equation 7)}$$

t represents an instantaneous pseudo-time variable and τ is an additive time delay factor in terms of ANM-LD cycles. When $\tau = 0$, the equation reduces to the well-known time-independent (equal time) correlations ranging from -1 to 1. For τ values larger than 0, the same equation gives time-delayed correlations between $\Delta\mathbf{R}_i$ at time t, and $\Delta\mathbf{R}_j$ at later time t+ τ. The case of i = j yields the autocorrelations of residues at both equal and delayed times.

There are two main parameters in defining the correlation behavior; the time window of the conformational transition (part of the trajectory from which the conformations are extracted) and the time delay factor τ. These correlations thus reflect the cooperativity of residues within the time window of the transition pathway, as well as with the time delay factor applied in the case of time-delayed behavior. In time-delayed correlations, τ is the time (in ANM-LD steps) chosen to reflect order of events. Nevertheless, the calculations were repeated for different time windows and time delay values. The τ value at which the autocorrelations turns from positive to negative values provides the coupling between pre-mean and post-mean conformational dynamics. Time-delayed cross-correlations reveal the co-movements of lead (preceding) and lag (delayed) residues or group of residues. For any two residues *i* and *j*, if $C_{ij}(\tau) > C_{ji}(\tau)$ for a given time delay, the fluctuations of residue *i* precede the fluctuations of residue *j*. Since the conformational change of *i* precedes that of *j,* residue *i* is likely the driving residue and residue *j* is the driven one. When examining the time-delayed cross-correlations between functional domains/residues (e.g., ATP binding residues, coupling helices, gates, BtuF-docking sites) one can infer causality relations, e.g., whether ATP binding cause BtuF binding or vice versa.

GNM Transfer Entropy

As an additional measure of directionality in allosteric communication we performed GNM-based calculations of the transfer entropy (Hacisuleyman and Erman, 2017). However, instead of including all the modes, we used only the GNM modes that correspond to the four most frequently used ANM modes in BtuCD and three in MalFGK. Transfer entropy (TE (i,j) (τ)) provides an estimate of the direction of information flow between two residues i and j for a certain time delay τ. That is, the degree to which the present movement of residue i decreases the amount of uncertainty for the future movement of residue j. If, TE(i,j)(τ) > TE(j,i) (τ), then the dynamics of residue i affects the dynamics of residue j, meaning a causal directional relationship between residues i and j.

The transfer entropy TE(i,j) (τ) from $\Delta\mathbf{R}$i(t) of residue i at time t to that of $\Delta\mathbf{R}$j (t+τ) of residue j at time t+τ was formulated (Hacisuleyman and Erman, 2017) as:

$$T_{i\to j}(\tau) = S(\Delta R_j(t+\tau)|\Delta R_i(t)) - S(\Delta R_j(t+\tau)|\Delta R_i(t), \Delta R_j(t)) \quad \text{(Equation 8)}$$

where the conditional entropies are

$$S(\Delta R_j(t+\tau)|\Delta R_i(t)) = -\langle \ln p(\Delta R_i(0), \Delta R_j(\tau))\rangle + \langle \ln p(\Delta R_i(0))\rangle \quad \text{(Equation 9)}$$

$$S(\Delta R_j(t+\tau)|\Delta R_i(t), \Delta R_j(t)) = -\langle \ln p(\Delta R_j(0), \Delta R_j(\tau))\rangle + \langle \ln p(\Delta R_i(0), \Delta R_j(0), \Delta R_j(\tau))\rangle \quad \text{(Equation 10)}$$

The details of the formulations for time correlation of fluctuations above were given in (Hacisuleyman and Erman, 2017). Using Equation 8 in the latter reference, we present net entropy transfer $TE_{ij}(\tau)$-$TE_{ij}(\tau)$ values for BtuCD and MalFGK in Figure S7.

Visualization

All PDB based figures were created using PyMOL 1.3 (The PyMOL Molecular Graphics System, Version 1.3, Schrodingr, LLC.).

Vitamin B_{12} Utilization Assays

WT or Δ*metE* Δ*btuD::kan* cells, transformed with the indicated plasmids, were grown in Davis minimal medium depleted of methionine in the presence of 0.15 nM vitamin B_{12}. The optical density of the cultures was measured every 10 min for 19 h. As a positive control, methionine was added at 20 ug/ml.

QUANTIFICATION AND STATISTICAL ANALYSIS

The ANM-LD generated during this study uses an in-house program (https://github.com/prclab/anmld_mutant). In the hybrid framework of ANM-LD, is used for the ANM calculations and consecutive call-outs of energy minimization and LD simulation steps performed in Amber 11-Sander (Case et al., 2010) biomolecular simulation package.

Mean and standard deviations of virtual backbone rotation angles were estimated over n=100 steps (cycles) and plotted for each simulation using normfit and normpdf functions in Matlab (MathWorks, 2019) under Results & Discussion, Figure 3A. As described on Equation 1 (under Results & Discussion), means of WT (μWT) virtual backbone rotation angles over n=2 parallel simulations were calculated by circ_mean function and the angular deviations of mutants from these means were computed by circ_dist function of CircStat (Berens, 2009) toolbox in Matlab. The results are plotted on Figure 3B under Results & Discussion.

The methods used met the assumptions of the statistical approach.

DATA AND CODE AVAILABLITY

All codes generated during this study for performing ANM-LD simulations on BtuCD (WT and mutant), $MalFGK_2$ and PglK conformations (as exemplified with BtuCD parameters and files), and The Cumulative Absolute Angle Deviation Analysis on BtuCD mutant conformations are available at GitHub with the following link: https://github.com/prclab/anmld_mutant.